Ricardo Jorge Guerreiro Antunes

Licenciado em Engenharia Biomédica

Automatic delimitation of the clinical region of interest in ultra-wide field of view images of the retina

Dissertação para obtenção do Grau de Mestre em
Engenharia Biomédica

Orientador: André Damas Mora, FCT, UNL

Júri:

Presidente: Carla Quintão, FCT, UNL
Arguente(s): Pedro Vieira, FCT, UNL

Setembro, 2014

LOMBADA

Automatic delimitation of the clinical region of interest in ultra-wide field of view images of the retina

Ricardo Antunes

2014

Automatic delimitation of the clinical region of interest in ultra-wide field of view images of the retina.

Copyright © Ricardo Jorge Guerreiro Antunes, Faculdade de Ciências e Tecnologia, Universidade Nova de Lisboa.

A Faculdade de Ciências e Tecnologia e a Universidade Nova de Lisboa têm o direito, perpétuo e sem limites geográficos, de arquivar e publicar esta dissertação através de exemplares impressos reproduzidos em papel ou de forma digital, ou por qualquer outro meio conhecido ou que venha a ser inventado, e de a divulgar através de repositórios científicos e de admitir a sua cópia e distribuição com objetivos educacionais ou de investigação, não comerciais, desde que seja dado crédito ao autor e editor.

Acknowledgements

To my advisor I want to thank for letting me do this thesis, for giving me the independence to find my own solutions to the problems which were presented and mostly for the amazing patience and personality and for being there whenever I need to.

To Manuel Coelho I want to thank for the amazing electric kettle which proportionate the amazing tea to free both our minds in the beginning and for company provided on those afternoons.

To Nuno Figueiredo for all those shared nights in the UNL-FCT and great mood which end up revealing to be so important to make sure this thesis were finalized in time.

To all my friends who were always there to make sure I don’t got out of line to many times and to make sure I got out when needed, for all the advices and always being an example to follow I have to truly thank with all my heart.

And finally but definitely not least the greatest thank of all to my spectacular family who don´t even know that this work is half of them, for the encouragement and particularly to my awesome sister for all the support and for all the laughs provided but mostly for always being an amazing example for me to follow.

Abstract

Retinal ultra-wide field of view images (fundus images) provides the visualization of a large part of the retina though, artifacts may appear in those images. Eyelashes and eyelids often cover the clinical region of interest and worse, eyelashes can be mistaken with arteries and/or veins when those images are put through automatic diagnosis or segmentation software creating, in those cases, the appearance of false positives results.

Correcting this problem, the first step in the development of qualified automatic diseases diagnosis programs can be done and in that way the development of an objective tool to assess diseases eradicating the human error from those processes can also be achieved.

In this work the development of a tool that automatically delimitates the clinical region of interest is proposed by retrieving features from the images that will be analyzed by an automatic classifier. This automatic classifier will evaluate the information and will decide which part of the image is of interest and which part contains artifacts.

The results were validated by implementing a software in C# language and validated through a statistical analysis. From those results it was confirmed that the methodology presented is capable of detecting artifacts and selecting the clinical region of interest in fundus images of the retina.

Keywords: clinical ROI, fundus images, retina, artifacts, eyelashes, eyelids, automatic, "user-free", algorithm, software.

Resumo

Imagens de campo alargado da retina proporcionam a visualização de grande parte da mesma, no entanto grande parte das imagens apresentam artefactos. É frequente o aparecimento tanto de pestanas, como de pálpebras nas imagens cobrindo desse modo a zona de interesse clínico e, pior, podendo as pestanas ser confundidas com artérias ou veias, quando estas imagens são sujeitas a programas de diagnóstico ou segmentação automática.

Corrigindo este problema, estará dado o primeiro passo no desenvolvimento qualificado de programas automáticos de diagnóstico de doenças e dessa forma também de uma ferramenta objetiva livre de erros subjetivos associados à presença humana.

Neste trabalho é proposto o desenvolvimento de uma ferramenta que delimite automaticamente a região de interesse clínica retirando, das imagens, características. Características essas que serão apresentadas a um classificador automático que avaliará a informação e decidirá se esta pertence ou não à zona de interesse da imagem.

Os resultados foram validados através da implementação de um *software* em linguagem C# e foram confirmados segundo uma análise estatística. Desses resultados surgirá a confirmação de que a metodologia apresentada neste trabalho foi a correta para a deteção de artefactos e para a delimitação automática da região de interesse clínica em imagens do fundo da retina.

Palavras-chave: ROI clínico, imagens do fundo, retina, artefactos, pestanas, pálpebras, automático, "user-free", algoritmo, software.

Table of Contents

List of Tables

List of Figures

Acronyms

ANN - Artificial Neural Network

BRVO - Branch Retinal Vein Occlusion

DR – Diabetic Retinopathy

ETDRS – Early Treatment of Diabetic Retinopathy Study

FFT - Fast Fourier Transform

FN - False Negative

FP - False Positive

GUI - Graphical User Interface

HRVO - Hemi-central Retinal Vein Occlusion

NPV - Negative Predictive Value

PPV - Positive Predictive Value

ROI - Region Of Interest

SLO - Scanning Laser Ophthalmoscopy

TN - True Negative

TP - True Positive

1

Chapter 1. Introduction

Ultra-wide field imaging, more specifically OPTOMAP, due to its effectiveness and large view of imaging , is becoming more clinically accepted and used over the standard ETDRS (Early Treatment of Diabetic Retinopathy Study) method of 7 standard fields of imaging, as it allows for the capture of one single image covering about 200º of the retina's surface. With this technology it is possible to visualize the central and periphery of the retina in the same image (Figure 1.1).

(a) (b)

Figure 1.1 - Comparison between standard and ultra-wide field imaging of the retina. (a) ETDRS 7 standard field image (45°); (b) Ultra-wide field of view image.

However certain artifacts often appear in those pictures. Eyelashes by being visible and eyelids by covering part of the retina make an automatic diagnosis very difficult.

This thesis main goal is to delineate the area containing these artifacts, by identifying and classifying the main features in ultra-wide field of view images, thus allowing automatic diagnostic to perform without errors.

The following sections will introduce the theoretical concepts to fully understand this thesis work.

1.1 Human Eye

The human eye (Figure 1.3) can be considered as being composed by three layers involving the liquid center, *vitreous body* and *aqueous humor*, responsible for the refraction (Figure 1.2). The outer layer, responsible for the protection, is consisted by the *sclera* and the transparent *cornea*. The middle layer with mainly vascular functions is composed by the *choroid*, *ciliary body* and *iris*. The *retina*, responsible for the vision, is located in the inner layer (Davson, 1980).

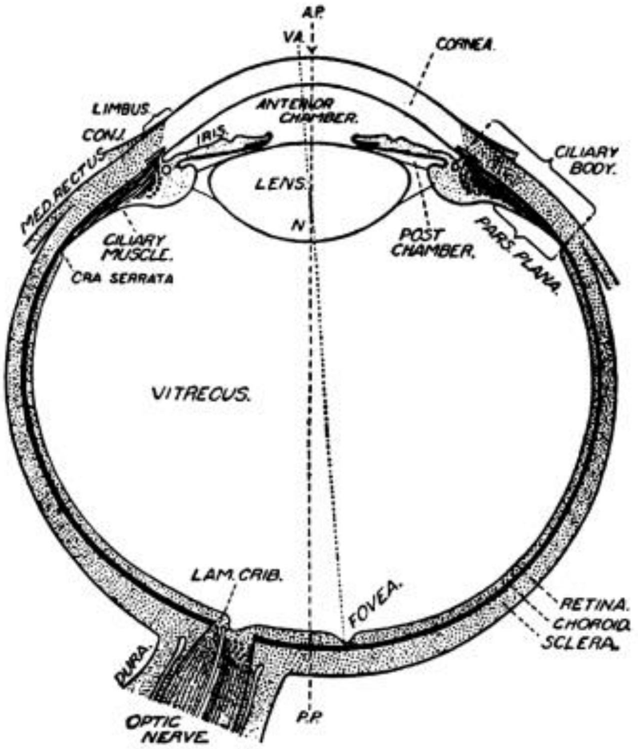

Figure 1.2 – Horizontal section of the eye. (Davson, 1980)

The *aqueous humor* main function is to provide the *crystalline lens* and the *cornea*, areas lacking blood vessels, with nutrients while the *vitreous body* function is to provide the necessary refraction and to fill the eye cavity. The *sclera*, composed by dense collagen fibers, holds together the contents of the eye and the *cornea* is responsible for most of the eye's focusing power. The *choroid*, rich in blood vessels, provides the nourishment for the retina's photoreceptors, the *ciliary body* and the *iris* make up the *uvea*, the *iris* open middle region is known as *pupil* and its size adjusts the level of light and accommodation (Lens, Nemeth, & Ledford, 2008).

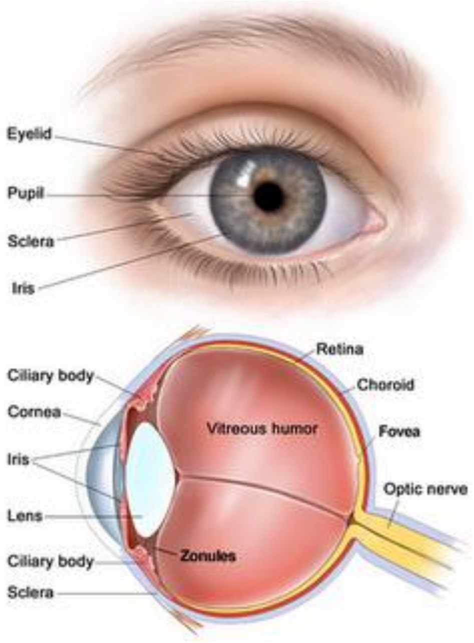

Figure 1.3 - Main components of the eye.

1.2 Retina

The retina is the part of the eye responsible for detecting light, transforming photon energy in electrical pulses that will later be interpreted by the brain. The retina has two kinds of photoreceptor cells, the rods and the cones. Rods are the most predominant (about 75 to 150 million cells) and they are very sensible to light but not to color, providing little detail. Cones are less abundant (about 6 to 7 million cells) and are very sensible to color but not to light, they are then responsible for the high resolution.

In the center of the retina there is a circular to oval white area measuring about 2x1.5 mm that is the optic disc which contains the optic nerve (here there aren't any photoreceptor cells, being then commonly known as "blind spot") from where the major blood vessels of the retina are radiated. At the left of the disc it can be seen a slightly oval-shaped, blood vessel-free reddish spot, the fovea, which is at the center of the area responsible for the central vision known as the macula. A circular field of approximately 6 mm around the fovea is considered the central area of the retina while from there is considered the peripheral area of the retina, stretching to the ora serrata (anterior boundary of the retina), approximately 21 mm from the center of the fovea. The total retina is a circular disc of between 30 and 40 mm in diameter (Figure 1.4).

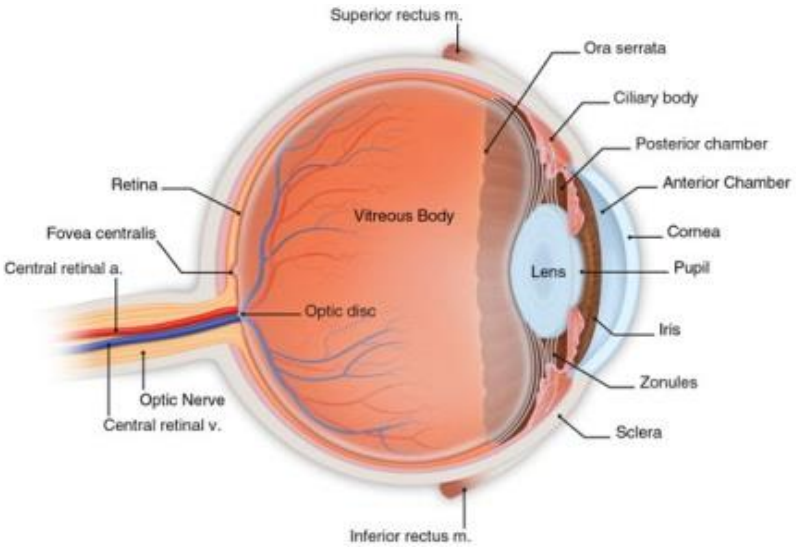

Figure 1.4 - Image of the eye and its components with special emphasis for the retina.

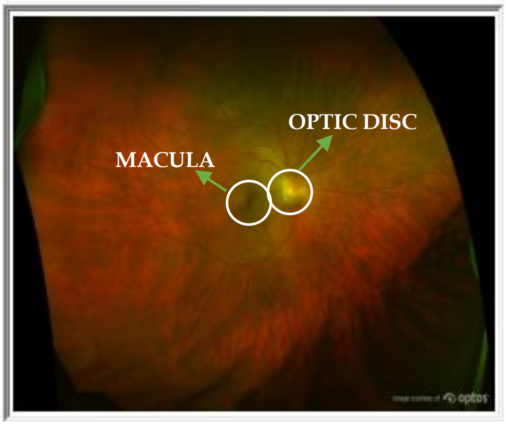

Figure 1.5 - Fundus image of the retina with the optic disc and macula in evidence.

1.3 Ultra-Wide Field Scanning Laser Ophthalmoscopy (OPTOMAP)

Ultra-wide field of view imaging (fundus imaging) technology allows that either the central and peripheral (less considered) parts of the retina to be visualized in the same image.

This technology of ultra-wide field scanning laser ophthalmoscopy (OPTOMAP) (Figure 1.6) when applied to the retina allows a 200º (Figure 1.7) retinal fundus image to be capture in a single picture, representing approximately 82% of the retinal area, with an acquisition time of 0.25 seconds, thus avoiding motion artifacts. This imaging is accomplished using scanning laser ophthalmoscope technology combined with the unique optical properties of an ellipsoidal mirror.

Figure 1.6 - OPTOS OPTOMAP MACHINE

One main characteristic of this technique is that it provides no real color images, i.e., it provides only two monochromatic red and green scanning laser ophthalmoscopy (SLO) scans that can be viewed separately or superimposed. This possibility to view the two, simultaneously generated red and green, SLO scans separately potentially provides additional image information. The green laser scan (Figure 1.8 (a)) may inherit more selective information about the superficial layers of the neurosensory retina, and the red laser scan (Figure 1.8 (b)) may better reflect the deeper retinal layers, including retinal pigment epithelium and choroid (Kernt et al. 2012).

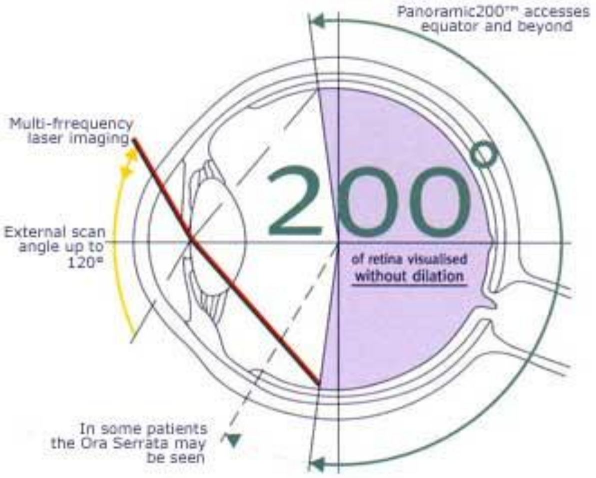

Figure 1.7 - Ultra-wide field imaging range given by OPTOMAP technology.

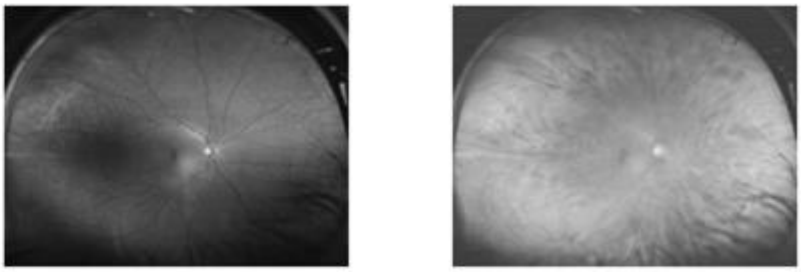
(a) (b)

Figure 1.8 - Comparison between the two monochromatic SLO, red and green scans. (a) Green channel image; (b) Red channel image.

With the development of current ultra-wide field imaging technology good image resolution and detail through the entire retina's surface has been achieved. The observation of fine retinal vascular lesions extending to the temporal and nasal periphery has been allowed with good results (Silva et al. 2013).

1.3.1 Peripheral Advantages/Applications

Ultra-wide field imaging offers many advantages in visualizing peripheral retinal pathology and in providing diagnostic evidence peripheral retinal pathologies, as it is believed that indicators of systemic diseases and precursors to different eye conditions often exhibit first on the retina periphery (Ortiz-rivera et al. 2007), that could not have been detected with clinical examination and standard ETDRS 7 field imaging.

There have been several reports using this technology in the management of patients with a wide variety of retinal disorders including diabetic retinopathy (DR) (Neubauer et al. 2008), sickle cell retinopathy, vein occlusion (BRVO/HRVO) (Cheng et al. 2008), retinal detachment, retinal vasculitis, cytomegalovirus (CMV) retinitis, retinal and choroidal tumors (Campbell et al. 2012) and classic cases of posterior and intermediate uveitis (Hong, Khanamiri, and Rao 2013). Also many retinal anomalies including retinal holes, retinal breaks and lattice degeneration can exist asymptomatically in the peripheral retina (Cheng et al. 2008).

Peripheral retinal vasculitis and non-perfusion, that might be difficult to appreciate on ophthalmoscopy, are easily seen with OPTOMAP imaging. Thus, proving that it could be a more clinically useful tool in detecting peripheral retinal vasculitis, or even the only tool needed for detection of vascular lesions in the retinal periphery (Hong, Khanamiri, and Rao 2013).

More specific delineation of retinal vascular non-perfusion in the far retinal periphery and detection of subtle areas of early peripheral neovascularization may be of particular clinical value (Prasad et al. 2010). The association between retinal vascular non-perfusion and retinal neovascularization may by an indication that zones of retinal non-perfusion may stimulate production of biochemical mediators leading to neovascularization (Patel et al. 2013) (McIntosh et al., 2007). Thus ultra wide-field imaging may be a powerful tool to identify therapeutic target areas for photocoagulation, allowing for efficient treatment of ischemic retina and potentially minimizing collateral destruction of viable perfused retina (Prasad et al. 2010).

Figure 1.9 - Ultra-wide field imaging of a normal retina.

Another main advantage of OPTOMAP imaging, especially regarding the wellbeing of the patient, is that it also allows for an eye examination under non-mydriatic conditions (without dilatation of the eye pupil) without any significative loss in sensitivity and specificity when compared with similar mydriatic exams (non-mydriatic exams are more comfortable for the patients) (Cheng et al. 2008) (Neubauer et al. 2008).

Thus, an increased view of the retina (Figure 1.9), not only covers more pathologies, but also allows a faster, earlier and more comfortable diagnostic, which in a long-term will provide an improved quality of life for the patient.

1.4 Important Retinal Diseases

1.4.1 Diabetic Retinopathy

Diabetic Retinopathy is a progressive disease that destroys capillaries in the eye, by slowly depositing abnormal material along the walls of the vessels in the retina (Figure 1.10).

In people with diabetes, some retinal blood vessels swollen which causes a higher blood flow that increases till the point of causing tiny leaks, that lead into hemorrhages, while the others blood vessels shrunken leading to a lower blood flow. The retina becomes then wet and swollen and cannot work properly. The form of diabetic retinopathy caused by leakage of the retinal blood vessels is called **Non-Proliferative Diabetic Retinopathy** (Figure 1.11 (a)).

Non-Proliferative Diabetic Retinopathy can be very uncomfortable and usually doesn't worsen over time but left unmonitored can lead into **Proliferative Diabetic Retinopathy**.

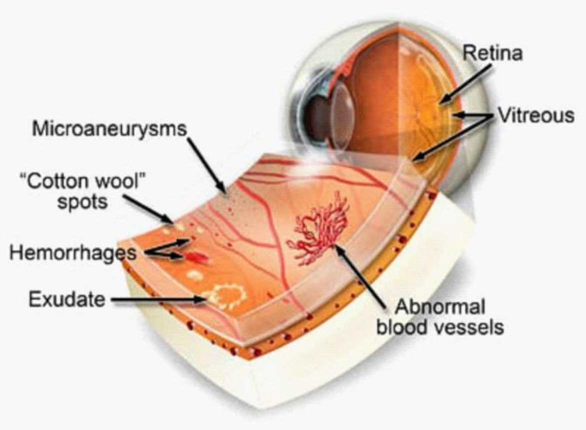

Figure 1.10 - Consequences of Diabetic Retinopathy.

Proliferative Diabetic Retinopathy (Figure 1.11 (b)) occurs in those vessels in which the blood flow decreases until it is closed. The retinal tissue which depends on those vessels for nutrition will no longer work properly. In those areas the affected retinal tissue produces molecules and these molecules then foster the growth of abnormal new blood vessels near the retina's surface, called neovascularization. This latter can be very bad for the eye because those new vessels can leak and bleed into the vitreous and even cause scar tissue that can result in blurred vision, later into blindness and even retina's detachment. **Proliferative Diabetic Retinopathy** continues, to this day, to be the major cause of blindness in the world.

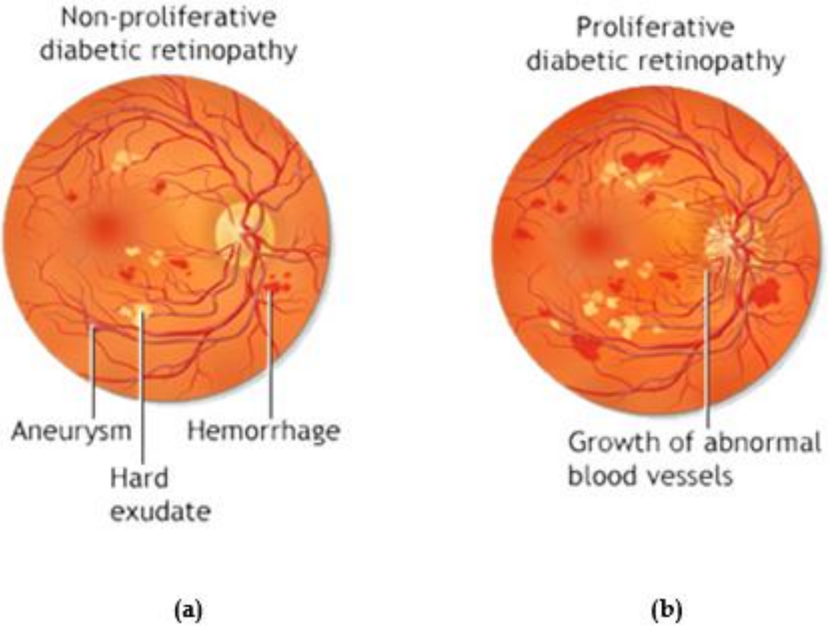

Figure 1.11 - Comparison between the two types of diabetic retinopathy. (a) Non-Proliferative Diabetic Retinopathy; (b) Proliferative Diabetic Retinopathy.

Diabetic Retinopathy Biomarkers

In order to have an early detection of DR we have to take into account biomarkers that are predicative of the disease. Looking for these biomarkers could affect the outcome in patients with diabetes, prevent visual loss and blindness and therefore reduce the morbidity and mortality (Cunha-Vaz, Ribeiro, and Lobo 2014) .

As we are assessing images, structural biomarkers is what we will study. More specifically, structural biomarkers are used both as risk estimators and for disease management, as they are reliable predictors of progression of retinopathy to more advanced stages.

Important structural biomarkers

One biomarker is the timely detection of “red lesions” such as micro aneurysms and hemorrhages, as they are reliable predictors of progression of retinopathy to more advanced stages. Another biomarker is the timely detection of “bright lesions” such as lipoprotein exudates and cotton-wool spots (Niemeijer et al. 2007).

Structural measurements also showed that diabetes leads to a retinal neuropathy independent of vascular DR. In patients with diabetes who do not have DR or who have only minimal DR, the thickness of the ganglion cell layer in the macula is decreased.

Diabetic Retinopathy through OPTOMAP

OPTOMAP offers several advantages for imaging the fundus in diabetic retinopathy (Figure 1.12). It is known that revealing areas of retinal ischemia, capillary non-perfusion and neovascularization are of considerable clinical importance as it is well established that those symptoms are likely to be predictive of the risk of diabetic macular edema (DME) which is a common cause of vision loss and decreased vision-related quality of in patients with DR (Manivannan et al. 2005).

Figure 1.12 - OPTOMAP image of an eye with Diabetic Retinopathy.

OPTOMAP imaging has been shown to reveal much more retinal non-perfusion more neovascularization than standard 7 field imaging (Wessel et al., 2012) even without the use of fluorescein angiography (Silva et al. 2013).

1.4.2 Branch Retinal Vein Occlusion

BRVO is associated with the high blood pressure. High blood pressure damages the veins in the eye thus affecting the overall vision. Therefore, a small percentage of people having BRVO also have an increased intraocular pressure (glaucoma). BRVO is a common cause of vision loss that affects approximately

1% of the population. It usually appears in middle-aged and elderly vasculopathic patients and can cause severe vision loss through macular edema, retinal neovascularization and retinal detachment.

More specifically if the damaged and blocked retinal veins are the ones that nourish the macula, some central vision is lost. In the majority of patients with vein occlusion, there are swelling of the central macular area and in about one-third of them, that macular edema will last for more than one year.

BRVO through OPTOMAP

Figure 1.13 - OPTOMAP image of an eye with BRVO.

It has been proved that OPTOMAP can be a useful tool in detecting peripheral retinal changes in people with BRVO (Figure 1.13), as it enables the detection of peripheral vascular non-perfusion and vascular leakage where peripheral non-perfusion may be associated with angiographic macular edema and therefore associated with BRVO (Prasad et al., 2010). It may also be able to detect some inflammatory markers which can be correlated with macular edema and size of BRVO (Tsui et al. 2013).

1.4.3 Uveitis

The uvea is the middle layer in the eye sandwiched between the retina (innermost layer) and the sclera (outermost layer). The uvea contains many blood vessels that carry blood to and from the eye. Uveitis is inflammation of the uvea.

Since the uvea nourishes many important parts of the eye, uveitis can damage the human vision.

Uveitis through OPTOMAP

OPTOMAP is a very useful tool in the diagnosis and management of uveitis having many advantages when compared with standard 7 field imaging (Figure 1.14).

By identifying patients with uveitis with higher sensitivity, ultra-wide field imaging can assist in determining more appropriate follow-up intervals, categorization of uveitis, and treatment (Hong, Khanamiri, and Rao 2013). It is also reasonable to use it to evaluate the periphery in patients with uveitis who maintain relatively good visual acuity (Hong, Khanamiri, and Rao 2013). More than ruling in the peripheral vasculitis, ultra-wide field imaging may play an essential role in ruling out such lesions in patients with uveitis (Hong, Khanamiri, and Rao 2013).

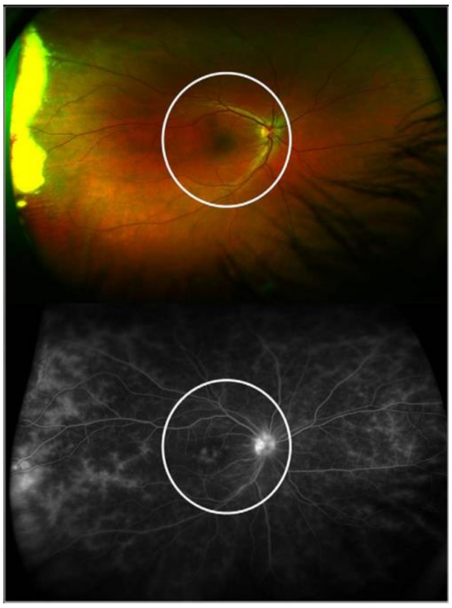

Figure 1.14 - OPTOMAP image of an eye with uveitis.

1.5 What is proposed in this thesis?

This thesis work proposes the use of image processing techniques and automatic classifiers to detect artifacts, mainly the eyebrows and eyelids, remove them and thereby selecting the retina region of interest from ultra-wide field of view images. As consequence is expected that this work will provide a tool to prevent false positives in automatic segmentation and diagnostic software and therefore making them more accurate, faster and efficient, providing a better quality for the patient.

There are very reports concerning the problems caused by eyelids and eyelashes. They appear in most fundus images covering and/or obscuring part of the region of interest of the image, mainly the superior and inferior regions (Jones 2004) (Silva et al. 2013). Then, by appearing in the image and, as eyelids and eyelashes resemble vessels, they create a large number of false positives in automatic software (Perez-Rovira et al. 2011) (Figure 1.15).

Figure 1.15 - Example of a fundus image with eyelashes and eyelids covering most of the ROI (region of interest) of the retina.

The proposed segmentation of eyelashes and eyelids will use mainly image processing techniques without the need of user intervention.

This thesis plan is to extract features from the several regions in the image describing their texture, color, focus and other characteristics, after an image preprocessing stage (setting brightness and contrast to proper values). The calculated features will be used with an automatic classifier, to classify then as *include* or *reject* those regions from the region of clinical interest. After post-processing to eliminate outcasts regions, the next step will be to delineate the passible area for processing, blurring the region of no interest emphasizing the region of clinical interest in the image.

The results will be obtained applying the software to a group of fundus images. Then they will be compared with manually marked images for evaluating the software performance (Figure 1.16).

Figure 1.16 - Example of an expected result of the software proposed in this thesis.

1.6 Thesis structure

In the following chapter a literature review of the related works will be done. In chapter 3 a full cover of the methodology of the automatic delimitation of the clinical ROI program will be shown, making a full description of all the methodology steps. Next, in chapter 4, will be shown how the methodology can be validated. Finally, the results will be assessed in chapter 5, followed by the conclusions in chapter 6.

2

Chapter 2. Literature Review

In order to have a proper execution of this work, a review of the previous works made in the area of segmentation, detection and/or suppression of either eyelids or eyelashes had to be accomplished. Only after recognizing the evolution of the works done in this area, a possible solution could be proposed.

2.1 Segmenting Eyelids

Several techniques and algorithms have been used to proper segment and detect eyelids, not exactly on OPTOMAP images though.

One of the first ones was an algorithm that divided eyelids from the localized iris regions by using a horizontal line (Masek, 2003), which was later improved by using two straight lines instead (Liu et al., 2005).

Advanced algorithms were later made which were able to detect and recognize parabola-shaped eyelids by using gray values measured in a counter-clockwise direction (Maenpaa, 2005) or by using canny edge detectors in which the longest detected edges were connected to the others (Chen et al., 2006) or even by some more advanced techniques which were able to detect eyelid candidate points by using a mask and locate eyelid line by using the Hough transform (Jang et al., 2007).

Techniques as clustering (ex: K-means clustering, fuzzy C-means clustering) have been used to proper select and classify regions in algorithms based on dividing the iris region into sub-blocks (Bachoo & Tapamo, 2005) or combined with an improved Hough transform to create a limbic boundary algorithm (Li et al. 2010).

The more complex techniques use algorithms such as least square fitting based on the detected eye corner positions (Vezhnevets et al., 2003) or rotatable parabolic Hough transform to detect eyelids (Jang, Kang, and Park 2008).

2.2 Segmenting Eyelashes

Segmentation and detection of eyelashes is more challenging when compared with eyelids therefore the techniques used are more recent and complex. These techniques were not initially accomplished for OPTOMAP images.

One of the first algorithms was based on the fact that the region containing many eyelashes had a large variation in gradient direction so eyelashes were detected and restored by a non-linear conditional directional filter (Zhang et al., 2006).

Another method for detecting eyelashes was based in using the edge information extracted by a phase congruency, which were invariant to the change of illumination. The detected eyelash region was restored by a simple inpainting technique using the four pixels nearest to the block containing the eyelash region (Huang et al., 2004).

More advanced techniques were later created, such as measuring the focus score of an iris image using a 5x5 convolution kernel and then use the focus score to select the threshold of local variance as well as sizes of the local window and convolution kernel for detecting the eyelash (Kang & park, 2007) and using four masks (and four directions) for eyelash line detection (Jang, 2003).

For better results in separating the eyelash region OTSU automatic thresholding have been successfully used (Min and Park 2009).

Nowadays the increased complexity of the techniques and algorithms has been achieved in order to properly detect and segment eyelashes.

2.3 *Segmenting eyelids and eyelashes in OPTOMAP*

When searching for papers in this area only a couple works were found that could resemble the kind of project this work is proposed to do.

The first paper was based on the "addition of a penalization step, run after vessel enhancement using steerable filters, in order to improve the segmentation of peripheral vessels and reduce the false positives on the region around the optic disc, choroidal circulation and lesion areas" (Perez-Rovira et al. 2011).

In the second paper the authors have used an automated image-pair registration method known as the Generalized Dual-Bootstrap Iterative Closest Point (GDB-ICP) algorithm to suppress the eyelash artifact in ultra-wide field retinal images. The percent of eyelash suppression shown in that study was about 6% regarding the overall image (Ortiz-rivera et al. 2007).

The first didn't focus on segmenting eyelids or eyelashes but showed results in reducing false positives, the second only focus on segmenting eyelashes, but revealed good results on doing it in ultra-wide field retinal images.

2.4 *Discussion*

The more complex techniques and algorithms of eyelid segmentation have demonstrated some degree of efficiency but require a great power of processing whereas the faster basic ones revealed elevated rate of malfunction on properly segment eyelids and even though several eyelid segmentation techniques were shown above they weren´t made for ultra-wide field imaging but for ETDRS 7-field standard photography.

Eyelash segmentation and detection is a more complex process therefore the techniques and algorithms presented before are also more complex. Though, some of them were already made for ultra-wide field imaging and showed results on identifying and suppressing eyelashes, however those results weren't faultless and were mainly based on mathematic algorithms.

Its notorious then the lack of work done in segmenting and detecting eyelids and eyelashes in ultra-wide field imaging. Knowing that eyelashes and eyelids create a large number of artifacts in the images a door has been open for an idea and a plan to be created.

3

Chapter 3. Methods of Detection

This work's goal is to supply ophthalmologists, more specifically those who work with automatic diagnosis and segmentation software, a tool that reduces error and facilitates and accelerates all processes, from the image acquisition through the final ophthalmologist evaluation. By helping those automatic diagnosis software to a proper execution, this work will eventually help providing a uniform criterion independent of the clinician who is executing the program. Therefore, the automatic identification of the clinical ROI do not represent a tool to perform an automatic diagnosis, but a tool to provide clinicians and ophthalmologists an easier and more accurate image analysis.

The ultra-wide field of view images (fundus images) used in this thesis are very complex and no two are alike: some have many artifacts others less; some are greener others redder; some have lesions others not; some have the retina focused (more common) others have the artifacts. Despite all this differences, this work was developed to overcome them and to accept all images not matter their particular features.

Figure 3.1 - Methodology for automatic delimitation of the clinical ROI in ultra-wide field of view images of the retina.

The methodology for automatic delimitation clinical ROI in fundus images is composed by three steps: image processing; region classification; image post-processing (Figure 3.1). In this chapter all this steps and its methods will be described.

3.1 The Methodology

There are usually an order for processing digital images, although in this thesis the order of the methods and the methods themselves were chosen simply by the results obtained.

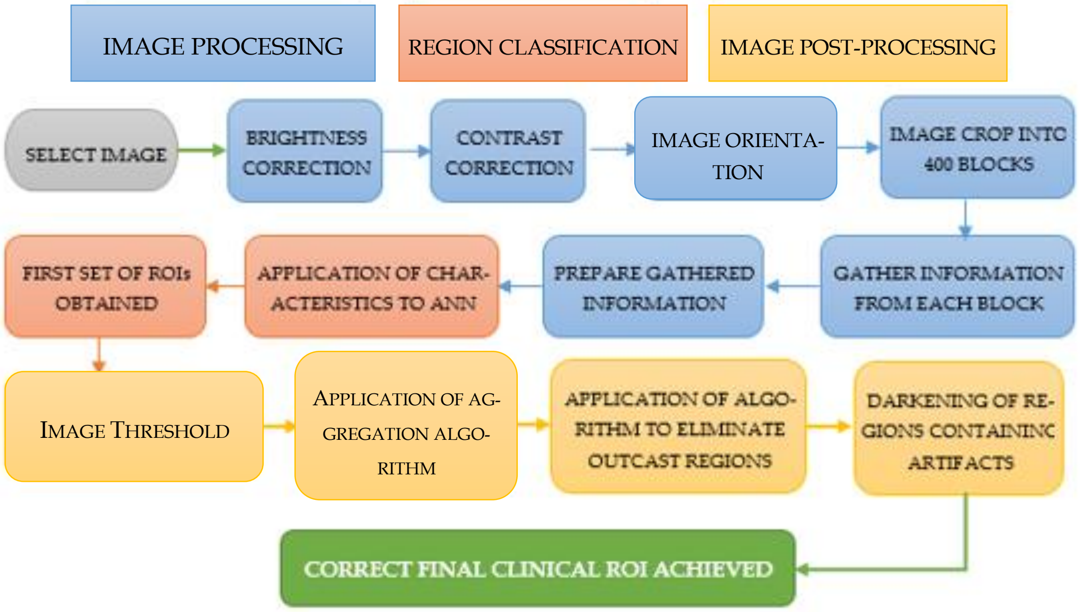

Figure 3.2 - Complete process (step by step) for automatic delimitation of the clinical ROI in ultra-wide field of view images of the retina.

After many attempts, the sequence in Figure 3.2 was ultimately the most promising one, the one that offered the better results, starting with the *image processing* methods, then with the *region classification* methods and finally with the *image post-processing* methods to achieve the final clinical ROI.

The *image processing* phase contains only low-level image operations to prepare the image for the next phase. The *region classification* phase is characterized by presenting four, empirically found, specific image features – red channel pixel intensity which had the ability to correctly find positive regions (regions correctly selected as being part of the clinical ROI); red channel lowest pixel intensity which presented similar results finding positive and negative regions; green channel pixel intensity which also presented similar results finding positive and negative regions; both channel FFT magnitude of the image which had the ability to correctly find negative regions (regions correctly selected as not being part of the clinical ROI)- to four artificial neural networks (ANNs), one for each of the specific image features, from which, a resulting ROI will be provided. The automatic classifier used in this thesis (Artificial Neural Network) was selected based on the ability that it presented in finding correlations between features through specific training. Besides those four selected specific features, more data have been assessed as more image features have been studied: image focus (each or both channels and channel ratios); image transitions (horizontally and/or vertically from each channel); intensity ratios (each or both channels); histogram ratios (each or both channels); highest and lowest pixel intensity (each channel). For each of those image characteristics an ANN were also created and trained as well as an ANN with all features and an ANN with some of the features. Ultimately, a specific ANN for each of those four selected features were found to be the better solution.

These results will then be sent to the *image post-processing* phase which finds isolated regions using morphologic algorithms, connects all ROI regions produced in the previous phase and organizes them into one clinical ROI. The final processed image is then suited for automatic diagnosis and later for ophthalmologists to assess it.

In the next subchapters the phases and methods will be further detailed and described.

3.2 Image Processing

The *image processing* phase is characterized by simple processes (Figure 3.3) whose main objective is to prepare and suit the image for the next phase, the *region classification*.

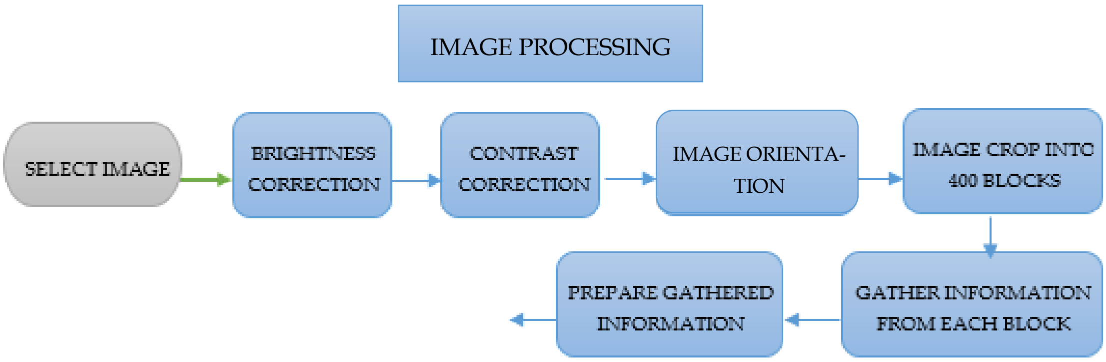

Figure 3.3 - Image pre-processing phase with all its methods and stages detailed.

It starts with two methods, brightness and contrast correction, whose goal is not to improve the image for a better visualization, but to improve the image for better results, what does not necessarily have to mean the same. The next stage, image orientation, ensures that the image has always the same orientation (optic disk on the right side). This stage is divided in three stages: image crop into 400 blocks; gather information from each block; and prepare the gathered information.

3.2.1 Brightness and Contrast Correction

The brightness and contrast correction was made individually for each of the four specific features as each of them require a different image treatment to provide the best possible result on its artificial neural network.

Figure 3.4 - Original image before the brightness and contrast correction.

On Table 3.1 are presented the results of evaluating the *red channel lowest pixel intensity by block* feature without any specific image treatment. As it is shown the FP error is very acceptable while the FN error is somewhat exaggerated. Assessing this data the image needed to present less contrast and more brightness (Figure 3.5) to evidence the eyelashes from the *red channel lowest pixel intensity by block* "point of view".

Table 3.1 - Results of red channel lowest pixel intensity before the brightness and contrast correction.

IMG	ERROR	
	RED CHANNEL	
	LOWEST INTENSITY VALUE	
	FP	FN
ERROR P/ ANN (%)	0,3778	2,2000
TOTAL ERROR P/ ANN (%)	2,5778	

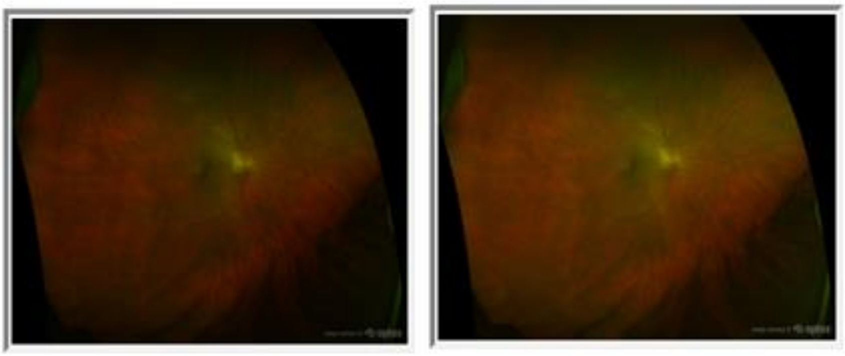

(a) (b)

Figure 3.5 - Original image after brightness and contrast correction. (a) Original image after the contrast being decreased; (b) Original image after the contrast being decreased and brightness being increased.

Table 3.2 -Results of red channel lowest pixel intensity after the brightness and contrast correction.

IMG	ERROR	
	RED CHANNEL	
	LOWEST INTENSITY VALUE	
	CONTRAST: -75%; BRIGHTNESS: 10%	
	FP	FN
ERROR P/ ANN (%)	0,4556	1,1000
TOTAL ERROR P/ ANN (%)	1,5556	

The results in Table 3.2, after brightness and contrast correction, show an almost identical but slightly worse FP error when compared to the previous one, but the FN error demonstrate a great decrease which leads to a much acceptable total error. These results validate the corrections made to the brightness and contrast in the original image for obtaining the proper *red channel lowest pixel intensity by block* feature.

Evaluating the first results of *red channel pixel intensity by block* characteristic without any specific image treatment in Table 3.3, it can be seen that the FP error and the FN error are both somewhat exaggerated which leads to a high total error. Assessing this data the image needed to present less contrast and less brightness (Figure 3.6) to evidence the artifacts (eyebrows and eyelashes) and not evidence the clinical ROI.

Table 3.3 - Results of red channel pixel intensity before the brightness and contrast correction.

IMG	ERROR	
	RED CHANNEL	
	AVERAGE PIXEL INTENSITY	
	FP	FN
ERROR P/ ANN (%)	0,8333	3,1889
TOTAL ERROR P/ ANN (%)	4,0222	

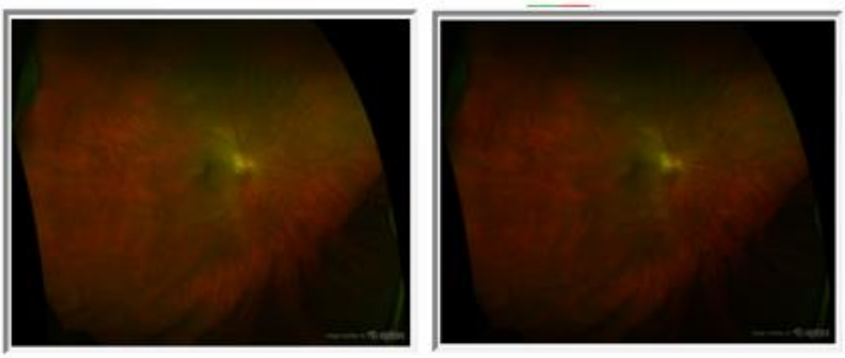

(a) (b)

Figure 3.6 - Original image after brightness and contrast correction. (a) Original image after the contrast being decreased; (b) Original image after the contrast and brightness being decreased.

The results in Table 3.4, after brightness and contrast correction, show a better FP error when compared to the one before brightness and contrast correction, and a much better FN error which leads to a much more acceptable total error validating the corrections made to the brightness and contrast in the original image for obtaining the proper *red channel pixel intensity by block* feature.

Table 3.4 - Results of red channel pixel intensity after the brightness and contrast correction.

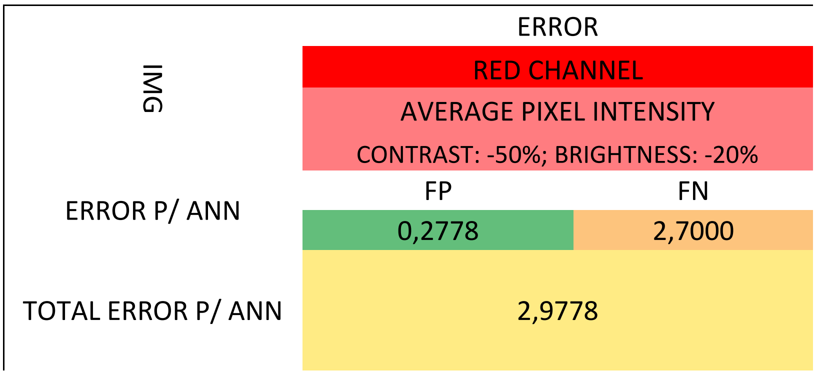

IMG	ERROR	
	RED CHANNEL	
	AVERAGE PIXEL INTENSITY	
	CONTRAST: -50%; BRIGHTNESS: -20%	
	FP	FN
ERROR P/ ANN	0,2778	2,7000
TOTAL ERROR P/ ANN	2,9778	

In Table 3.5 are evaluated the first results of *green channel pixel intensity by block* feature without any specific image treatment. Here the FP error is too high while the FN error is very acceptable which leads to a high total error. Assessing this data the image needed to present a little less contrast and much less brightness (Figure 3.7) to be able to detect the artifacts (eyebrows and eyelashes).

Table 3.5 - Results of green channel pixel intensity before the brightness and contrast correction.

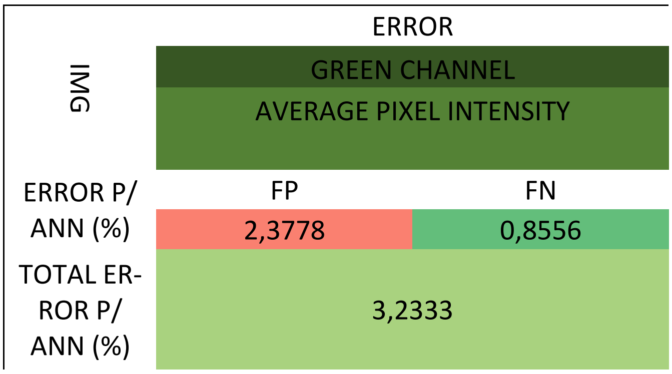

IMG	ERROR	
	GREEN CHANNEL	
	AVERAGE PIXEL INTENSITY	
	FP	FN
ERROR P/ ANN (%)	2,3778	0,8556
TOTAL ERROR P/ ANN (%)	3,2333	

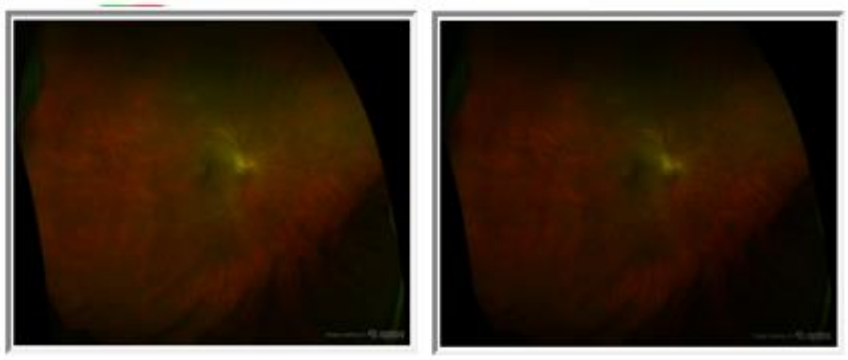

(a) (b)

Figure 3.7 - Original image after brightness and contrast correction. (a) Original image after the contrast being slightly decreased; (b) Original image after the contrast and brightness being decreased.

The results in Table 3.6, after brightness and contrast correction, show a much improved FP error when compared to the previous one, before brightness and contrast correction, and a slightly increase in the FN error which, ultimately leads to a much more acceptable total error validating the corrections made to the brightness and contrast in the original image for obtaining the proper *green channel pixel intensity by block* feature.

Table 3.6 - Results of green channel pixel intensity after the brightness and contrast correction.

IMG	ERROR	
	GREEN CHANNEL	
	AVERAGE PIXEL INTENSITY	
	CONTRAST: -25%; BRIGHTNESS: -20%	
ERROR P/ ANN (%)	FP	FN
	0,6222	1,7479
TOTAL ERROR P/ ANN (%)	2,3701	

Evaluating the first results of *FFT magnitude by block* feature without any specific image treatment in Table 3.7, it can be seen that the FP error is almost perfect while the FN error is extremely high which leads to a high total error.

Assessing this data the image needed to present much less contrast and more brightness (Figure 3.8) to not over detect the clinical ROI.

Table 3.7 - Results of magnitude FFT before the brightness and contrast correction.

IMG	ERROR	
	FFT MAGNITUDE	
	FP	FN
ERROR P/ ANN (%)	0,0778	7,8889
TOTAL ERROR P/ ANN (%)	7,9667	

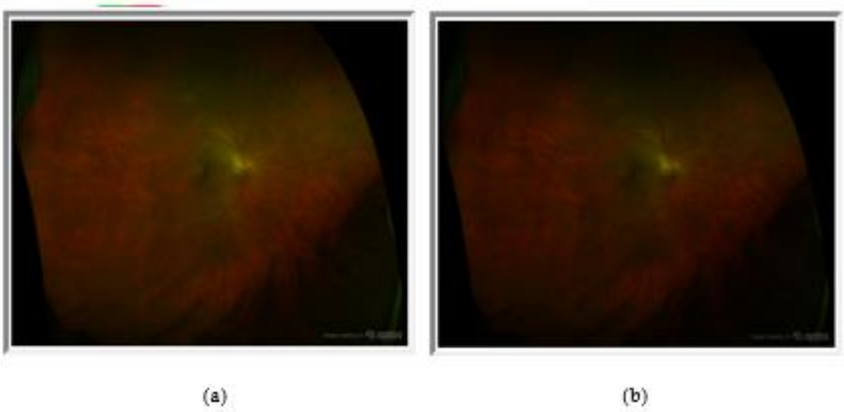

Figure 3.8 - Original image after brightness and contrast correction. (a) Original image after the contrast being decreased; (b) Original image after the contrast being decreased and brightness being increased.

The results in Table 3.8, after brightness and contrast correction, show an increased FP error when compared to the previous one, before brightness and contrast correction, to compensate the extremely drop in the FN error which, ultimately leads to a much more acceptable total error approving the corrections made to the brightness and contrast in the original image for obtaining the proper *FFT magnitude by block* feature.

Table 3.8 - Results of FFT magnitude after the brightness and contrast correction.

IMG	ERROR	
	FFT MAGNITUDE CONTRAST: -75%; BRIGHTNESS: 0.7%	
	FP	FN
ERROR P/ ANN (%)	0,4778	2,5444
TOTAL ERROR P/ ANN (%)	3,0222	

These results demonstrate the importance of the brightness and contrast correction throughout the characteristics in study as the total error have shown a decrement for all the specific image characteristics in study while maintaining the FP error, more important, virtually nil.

3.2.2 Image orientation

Before retrieving all the information necessary for *image processing* and as the blocks' location on the image have an important role as block feature, it is crucial to have all the images oriented similarly. The most common problem is that left and right eyes have the optic disk in opposite horizontal locations and for automatic image analysis this should be corrected. This step is then responsible to orientate all images using the same final criteria.

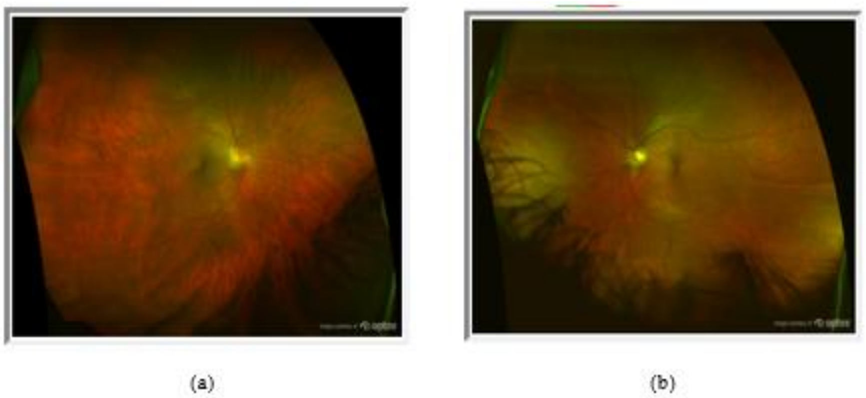

Figure 3.9 - Two images with different orientations. (a) Image with an orientation considered normal for this works purpose; (b) Image with an orientation considered inverted for this works purpose.

In this work an image is considered correctly oriented when the optic disc is located on the right side of the image (Figure 3.9 (a)) and when it is inverted it is considered with an incorrect orientation. When the image has an incorrect orientation a horizontal flip is necessary.

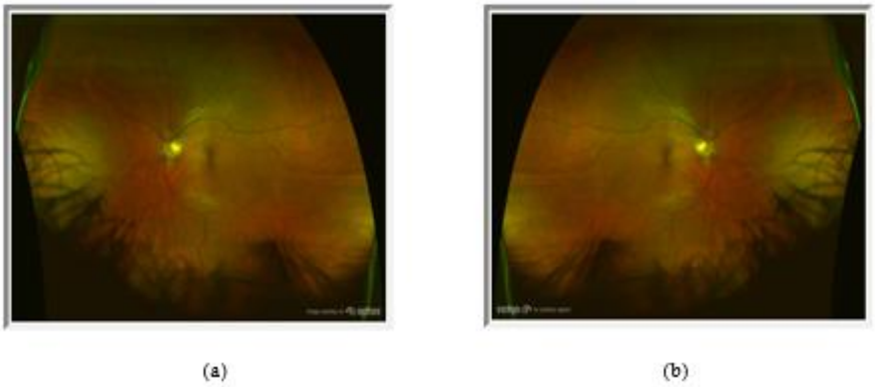
(a)
(b)

Figure 3.10 - Reversing the orientation of the image. (a) Original image; (b) Original image correctly inverted.

To automatically invert the image when it is necessary, the image is divided into 225 blocks (15x15) and is checked if the block that has the highest green channel pixel intensity, representing the block that contains the optic nerve, is on the left side of the image, if so then the image is flipped horizontally (Figure 3.10), otherwise it remains in its original orientation.

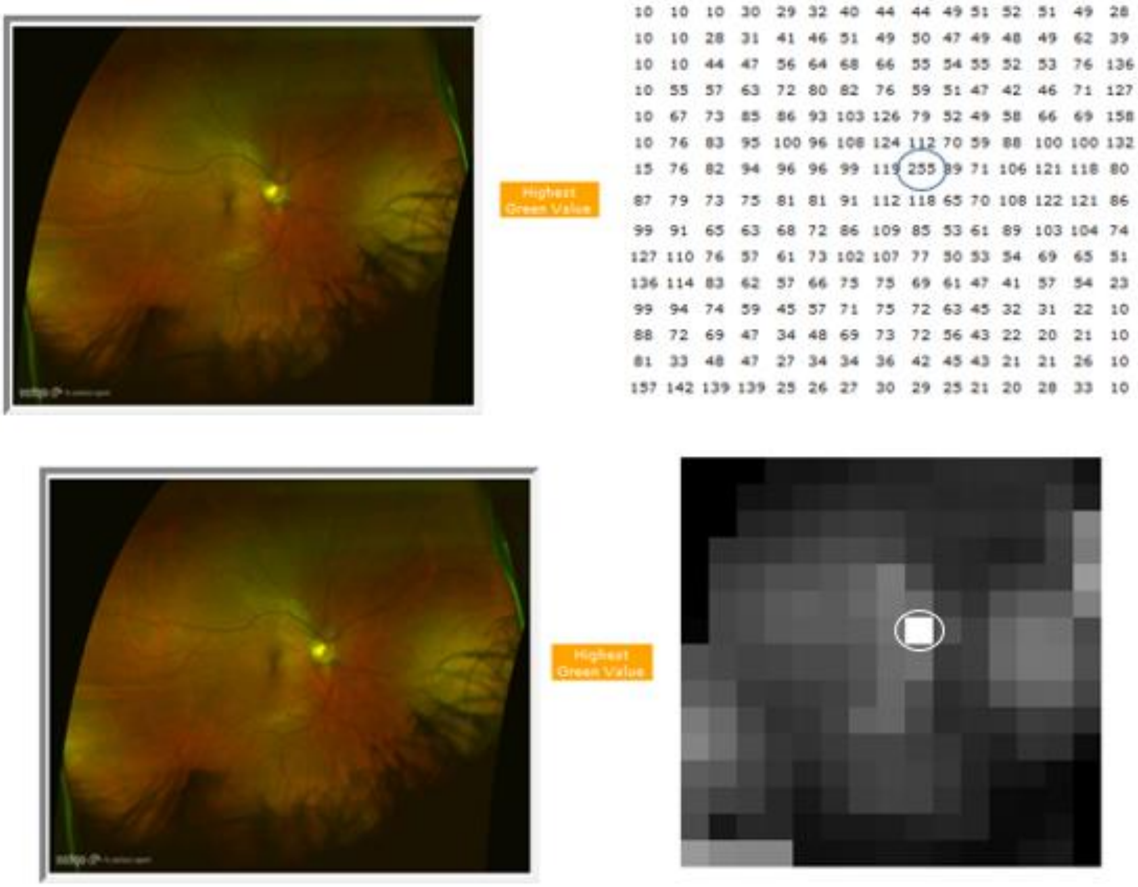

10	10	10	30	29	32	40	44	44	49	51	52	51	49	28
10	10	28	31	41	46	51	49	50	47	49	48	49	62	39
10	10	44	47	56	64	68	66	55	54	55	52	53	76	136
10	55	57	63	72	80	82	76	59	51	47	42	46	71	127
10	67	73	85	86	93	103	126	79	52	49	58	66	69	158
10	76	83	95	100	96	108	124	112	70	59	88	100	100	132
15	76	82	94	96	96	99	119	255	89	71	106	121	118	80
87	79	73	75	81	81	91	112	118	65	70	108	122	121	86
99	91	65	63	68	72	86	109	85	53	61	89	103	104	74
127	110	76	57	61	73	102	107	77	50	53	54	69	65	51
136	114	83	62	57	66	75	75	69	61	47	41	57	54	23
99	94	74	59	45	57	71	75	72	63	45	32	31	22	10
88	72	69	47	34	48	69	73	72	56	43	22	20	21	10
81	33	48	47	27	34	34	36	42	45	43	21	21	26	10
157	142	139	139	25	26	27	30	29	25	21	20	28	33	10

Figure 3.11 - Region containing the optic disc; Image above in values; Image below in colors.

3.2.3 Gathering and preparation of the characteristics

To gather the necessary information from all of the important characteristics to assess the final result, the image has to be divided into 400 (20x20) small images and each will be evaluated (Figure 3.12).

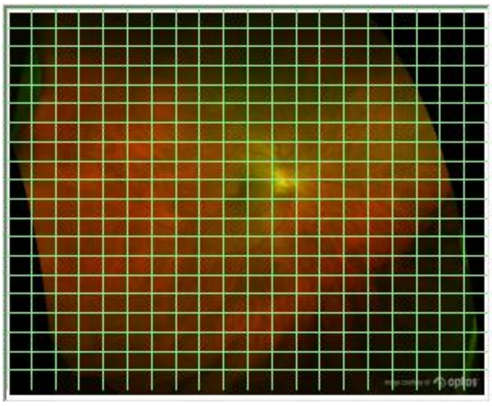

Figure 3.12 - Image divided into 400 (20x20) small images.

Each of the 400 images is evaluated and from each one are acquired the distance to the center of the original image, the red channel pixel intensity (Figure 3.13), the red channel lowest pixel intensity, the green channel pixel intensity and the FFT magnitude.

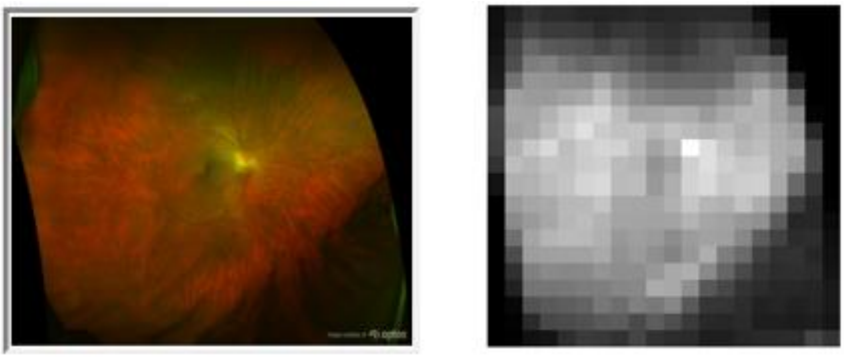

Figure 3.13 - Red channel average pixel intensity values per block.

Since artificial neural networks have a better convergence when the inputs are in the [0…1] interval, the information is then normalized to this interval by dividing by the maximum feature value. The information is now fully prepared to be subject to the *region classification* phase.

3.3 Region Classification

In this stage the information is presented to previously trained automatic classifiers, capable of read the specific information previously treated, evaluate it and to provide a set of ROI's as a response.

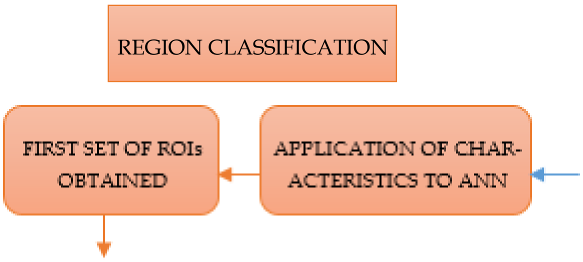

Figure 3.14 - Structure of the image processing phase and its methods.

For this works purpose it was empirically found that using an artificial neural network (ANN) for each of the four specific characteristics (red channel pixel and lowest pixel intensity, green channel pixel intensity and FFT magnitude) provides the best results for an automatic classification. All ANN had the same geometry, all had four layers: one input layer, two hidden layers and one output layer; the input and hidden layers were each composed by two neurons while the output layer were composed by one. The neurons of the input layer were responsible for receiving the information containing the distance of the block to the center of the image and the information regarding the specific characteristic feature of the ANN. The neurons corresponding to the hidden layers were responsible for classifying the information and decide its direction. The neuron of the output layer were responsible for giving the result of that specific ANN and its result varied between 0 and 1 where a result close to 0 stood for a region of the image containing artifacts while a result close to 1 a region of the image that would be part of the clinical ROI (Heaton 2008).

All ANNs referenced above were trained with twelve images through the back-propagation method. From those twelve images were gathered information of the specific characteristics of the image also by cropping the image into blocks. At each block were attributed the value of 0 or 1 according to the image there, if the image contained part of an artifact at that block were attributed the value 0 if not at that block were attributed the value 1. Each ANN were trained by taking into account the value of judgment made.

Therefore, depending on the information entering the corresponding ANN a value close to 0 or 1 leaves the ANN providing, in that way, the first ROI of the image. As there are four different ANNs, for each of the specific characteristics, after this phase there will be four different ROIs. To join all this information more processing is require as the next phase, *image post-processing*, will demonstrate.

3.4 Image Post-Processing

The main goal for this phase is to aggregate all the information into one final clinical ROI with the minimum error possible, and preferably with no default error at all. In this phase an image resulting from an OTSU binarization will be one additional information to aggregate with the ones already obtained. After all the information is computed, the final image presented to the user is prepared by darkening the regions containing artifacts.

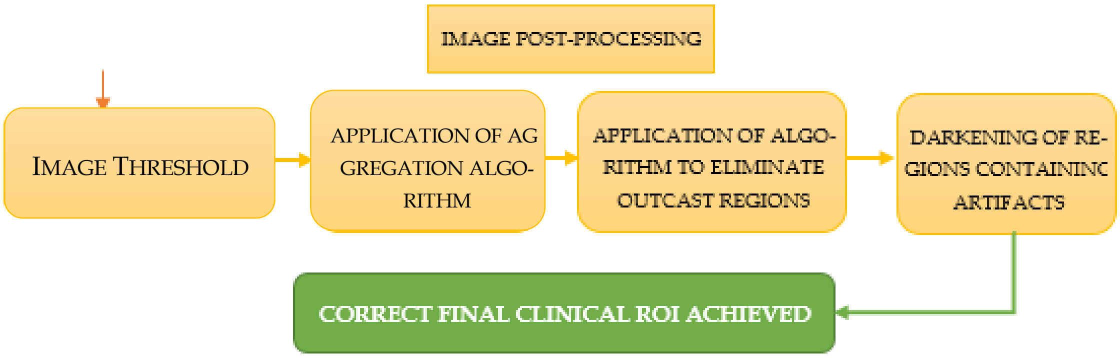

Figure 3.15 - Structure of the image post-processing phase and its methods.

3.4.1 Image threshold

For this step a normal OTSU binarization (Otsu 1975) containing the 256 pixel intensities is applied.

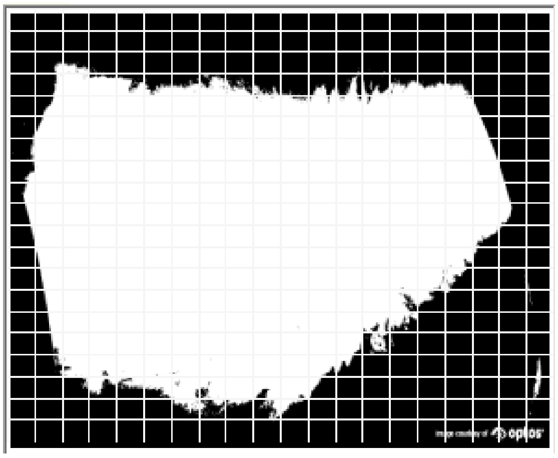

Figure 3.16 – Binarized image after OTSU Thresholding.

After the image is binarized the resulting image is cropped into 400 (20x20) blocks (Figure 3.16), just as for the specific characteristics. If the image in the block contains at least one pixel with zero intensity then this block is assigned the value 0 (contains artifacts) otherwise this block is assigned to the value 1 (part of the ROI).

3.4.2 Aggregation algorithm

After computing the five ROI required: red channel pixel intensity ROI, red channel lowest pixel intensity ROI, green channel pixel intensity ROI, the FFT magnitude ROI and the OTSU binarization ROI; the next step is to aggregate all of them into one single ROI.

The ROI aggregation algorithm analyses all individual ROI and for each one a rule has been empirically found to choose the real value for the final clinical ROI. If the value of the OTSU binarization ROI is 1 or all of the other ROIs are 1 the final value is 1 (part of the ROI) otherwise the final value is 0 (contains artifacts). This was the algorithm that achieved the better results, and whose results were more satisfactory, although it still contains problems, such as regions in the image center falsely selected as containing artifacts (final value 0) or regions in the image periphery falsely selected as part of the ROI (final value 1), corrected with the next algorithm.

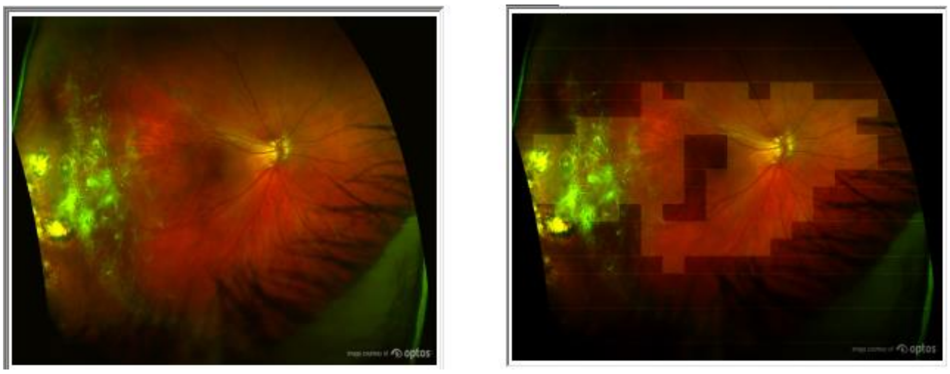

Figure 3.17 – Resulting ROI of aggregation algorithm.

3.4.3 ROI final post-processing

Having a first tentative ROI the next step is to find and eliminate regions falsely selected as containing artifacts or being part of the ROI.

In this step all ROI matrix regions are re-analyzed following the rule: if the region *contains artifacts* and if there are at least three regions surrounding it (above, below, left and/or right) *containing no artifacts* then the region is corrected as *containing no artifacts* too otherwise the region remains the same (Figure 3.18). After the ROI matrix have been completely analyzed and the region values corrected, this new ROI matrix is re-analyzed again with an extra condition, to check if there is a region *containing no artifacts* completely surrounded by regions *containing artifacts*, if so then the region is corrected to *containing artifacts*. In this final rule if there is a region *containing artifacts* in the center of the image it will correspond to the macula area and then the region is corrected to *containing no artifacts* (Figure 3.19).

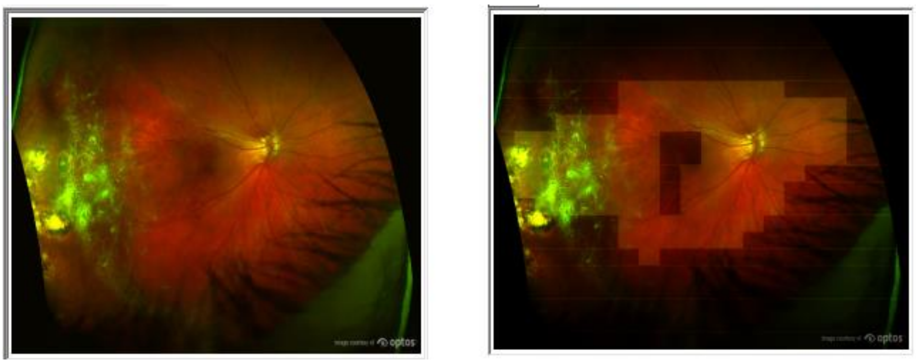

Figure 3.18 – First crossing resulting ROI.

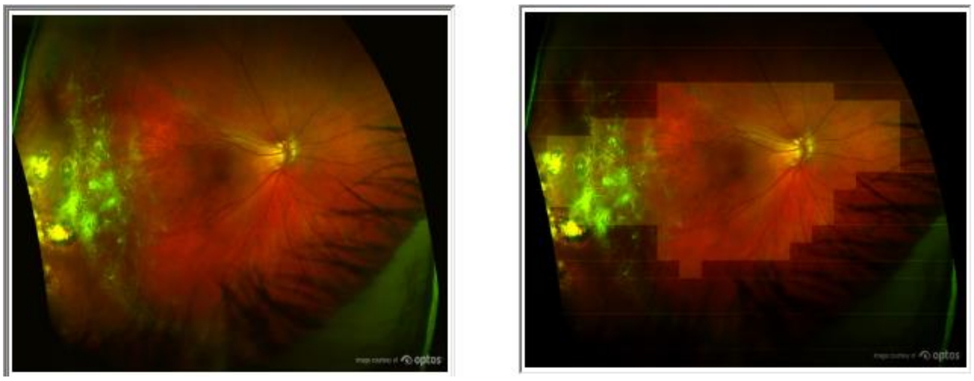

Figure 3.19 - Final crossing resulting ROI.

3.4.4 Darkening of the regions containing artifacts

The next step is to darken the regions containing artifacts (the regions corresponding to 0 in the final ROI). For that purpose a ROI matrix has been created containing only the regions having artifacts.

Finally, the brightness is reduced on those ROIs remaining in the ROIs matrix, thus creating a final image identical to the original one but with the regions containing artifacts darkened.

3.5 Summary

The presentation of the methodology for automatic delimitation of the clinical ROI in fundus images of the retina is now complete. As main methods in this methodology the *aggregation algorithm* and *ROI final post-processing* assume great importance.

The *aggregation algorithm* and *ROI final post-processing* altogether represent a new algorithm proposed in this work that showed to be a consistent way of post-processing the data with reliable results.

Concluding the methodology presentation the next chapter will focus on the software necessary to implement the algorithms.

4

Chapter 4. Methods of Validation

In this chapter is presented the tool developed for validating the proposed methodology. It implemented all algorithms describe before. The main goal when implementing this software was to create the more user friendly graphical user interface (GUI) possible and so that no previous user training is required. This software is better suited for complementing automatic diagnosis and segmentation programs, as it simple to implement and can be easily attached to those programs.

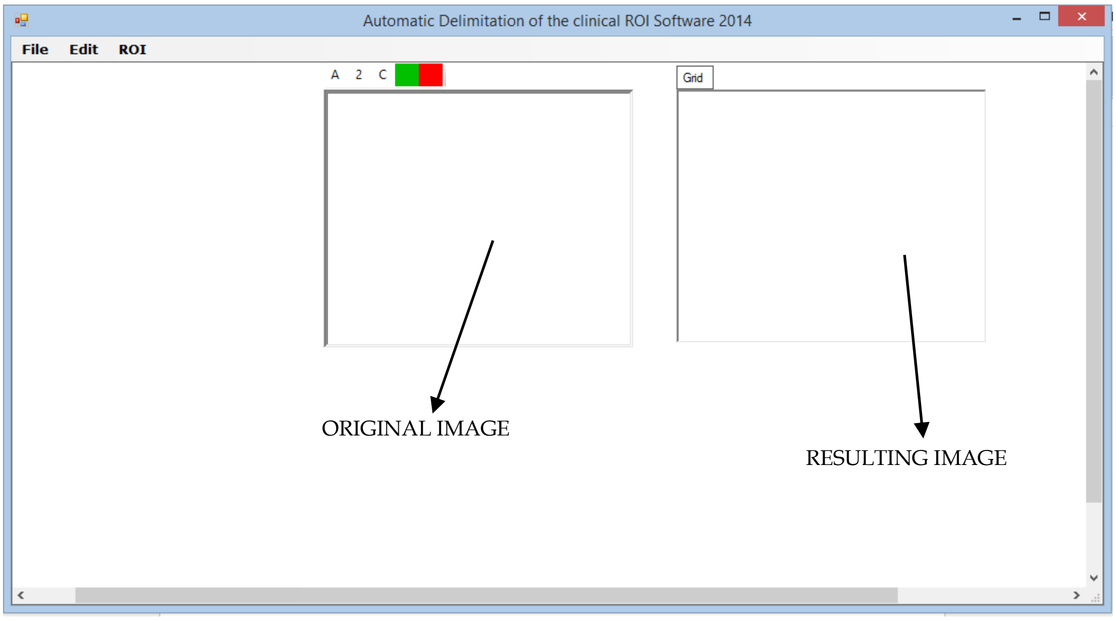

Figure 4.1 - Graphical user interface (GUI) of the automatic delimitation of the clinical ROI software.

Figure 4.1 shows the produced graphical interface. The resulting image will appear in the right, while the original image will remain on the left allowing a comparison between the two images and the results evaluation. To facilitate the assessment if one region of the image has been correctly darkened or if there was a region left to be darkened, a grid can be overlaid to the image (Figure 4.2).

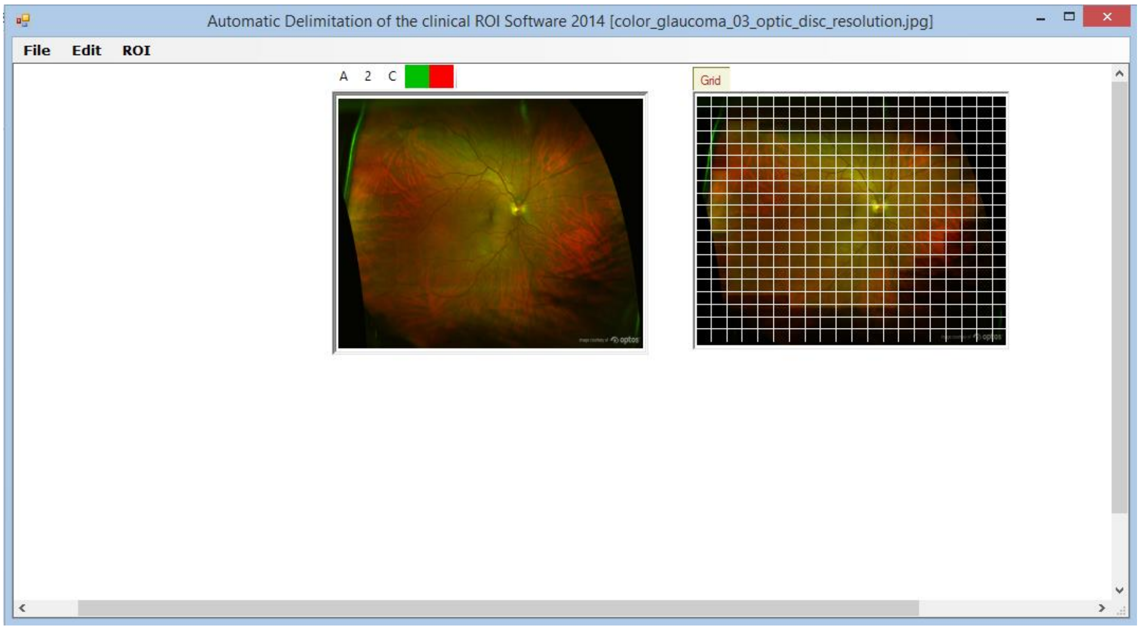

Figure 4.2 - Resulting image with the grid selected.

To validate the data an individual evaluation of each block in the resulting image is necessary, the results will be calculated after assessing each block of each image if it has been properly evaluated.

For a better understanding of the program and all its functions a more detailed explanation is given in the following sections.

4.1 GUI

The full description of the GUI will be divided in its design and its functionalities, which will be presented next.

4.1.1 Design

The GUI (Figure 4.3) is composed by:

- Two picture boxes, one for the original image and another for the resulting image;
- Two panels, one that shows all the images present in the working folder and another (history panel) that shows the images which already have been analyzed;
- Main menu containing three items:
    - File containing four menu items: Open Image; Open Folder; Save Image; Exit;
    - Edit containing an Undo menu item;
    - ROI containing a Final menu item.
- Grid button to show or remove the grid from the resulting image.
- Set of buttons to select how to see the original image: red channel, green channel, both images, image with both channels (original image) or the three images.

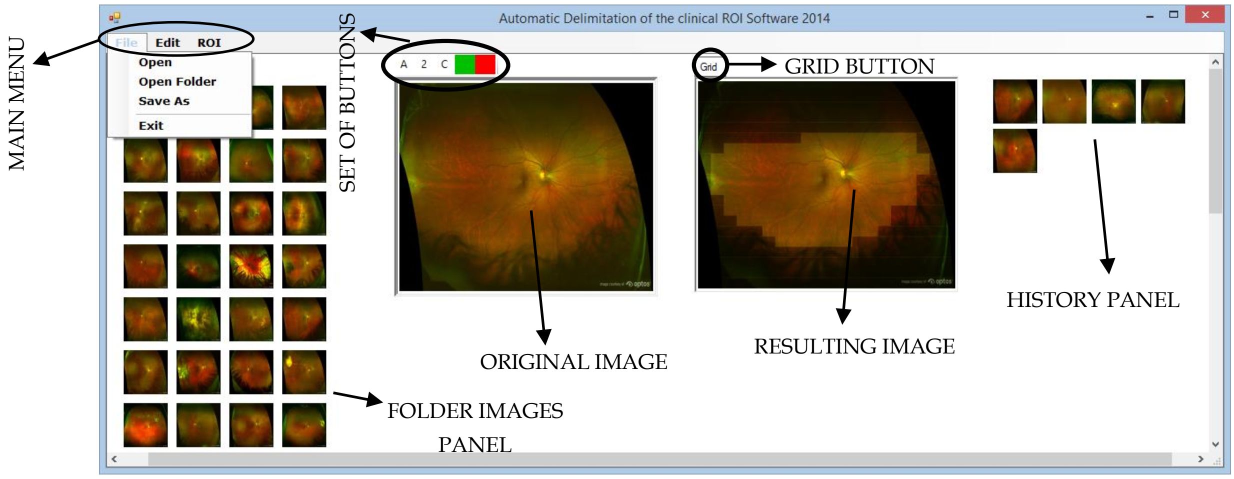

Figure 4.3 - Detailed GUI.

4.1.2 Functionalities

Before being ready to execute the program it is important to know the functions that aren't very explicit.

The *Open* menu item in the *FILE* menu opens a single image appearing in the *original image picture box*, instead the *Open Folder* menu item opens all images in a folder selected by the user and displays them in the *Folder Images Panel*. In this latter option if the user from the folder panel selects one image, it appears in the *original image picture box*. The *Save As* menu item in the *FILE* menu saves the image in the *resulting image picture box* with a name and file extension chosen by the user. The *Undo* item in the *EDIT* menu places the previous image in the *original image picture box*.

When a new image is sent to the *resulting image picture box,* the previous image is sent to the *history panel*. All images in the *history panel* can be assessed by clicking on them, appearing in the *resulting image picture box*.

By clicking on *Final* menu item in the *ROI* menu the image in the *original image picture box* will be processed and the its final ROI will be presented in the *resulting image picture box* with, approximately, one minute time delay.

Important note

To allow for the *ROI* menu function a primary evaluation had to be made before for studying purposes. As the original image were cropped into blocks a table and the image cropped would appeared below the *original image picture box* with the possibility of a value or color visualization of each image feature (Figure 4.4) and if a block was selected a list of its entire features were presented (Figure 4.5).

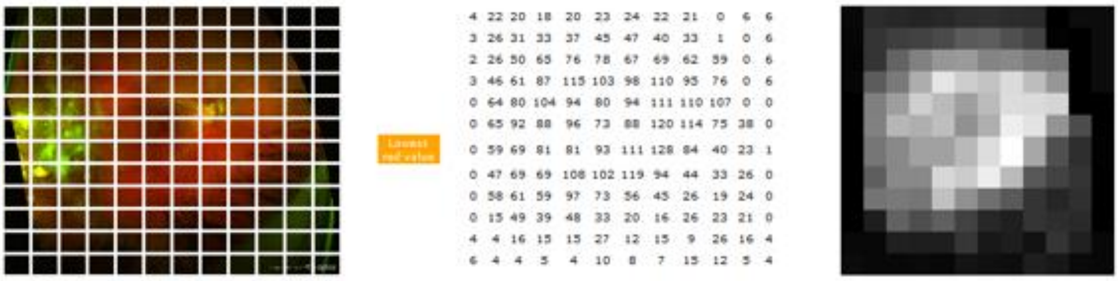

4	22	20	18	20	23	24	22	21	0	6	6
3	26	31	33	37	45	47	40	33	1	0	6
2	26	50	65	76	78	67	69	62	59	0	6
3	46	61	87	115	103	98	110	95	76	0	6
0	64	80	104	94	80	94	111	110	107	0	0
0	65	92	88	96	73	88	120	114	75	38	0
0	59	69	81	81	93	111	128	84	40	23	1
0	47	69	69	108	102	119	94	44	33	26	0
0	58	61	59	97	73	56	45	26	19	24	0
0	15	49	39	48	33	20	16	26	23	21	0
4	4	16	15	15	27	12	15	9	26	16	4
6	4	4	5	4	10	8	7	15	12	5	4

Figure 4.4 - Image cropped into 144 (12x12) blocks with value and color visualization of the red channel lowest pixel intensity value and color by block.

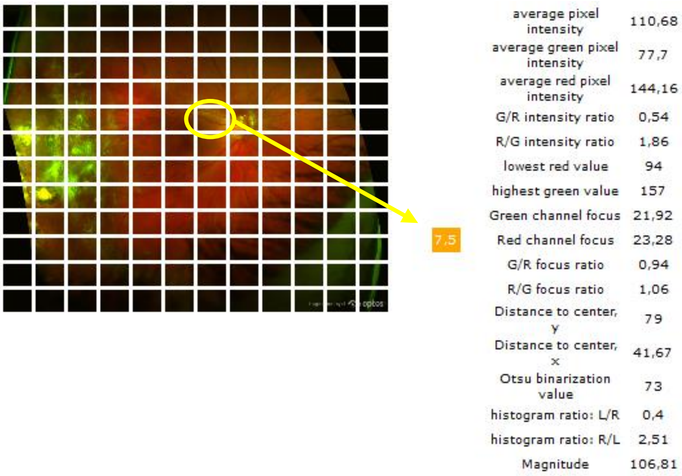

average pixel intensity	110,68
average green pixel intensity	77,7
average red pixel intensity	144,16
G/R intensity ratio	0,54
R/G intensity ratio	1,86
lowest red value	94
highest green value	157
Green channel focus	21,92
Red channel focus	23,28
G/R focus ratio	0,94
R/G focus ratio	1,06
Distance to center, y	79
Distance to center, x	41,67
Otsu binarization value	73
histogram ratio: L/R	0,4
histogram ratio: R/L	2,51
Magnitude	106,81

Figure 4.5 – Features list of the selected image block.

4.2 Summary

The software created achieved the objectives, as not only the program is user-friendly but also works as a validation method for the automatic clinical ROI delimitation. The program has few objects and each one has a tooltip with indications of what purpose it serves.

Comparing the images produced with the original ones, it is simple to assess of how good the clinical ROI is, with the help of the grid the data can be quantified and qualified and the associated statistical analysis be calculated.

5

Chapter 5. Results Evaluation

The results evaluation and the assessment of their efficiency was held by comparing the final clinical ROI with the expected one, checking block by block if the area has been correctly darkened. With the individual data of each image available, predictive values and statistical values, such as specificity and sensitivity, have been calculated.

In this work the specificity, the ability of a test to correctly classify the negatives, has more importance than the sensitivity, the ability of a test to correctly classify the positives, as such, a final table with those indicators is needed for a combined final assessment.

5.1 Materials and Methods

The images used to assess the accuracy of the automatic delimitation method were obtain from a fundus images database. The validity of the results were measured using a set of statistical measures, such as specificity and sensitivity.

5.1.1 Images Database

A set of 43 retinal fundus images from *OPTOS color fundus image library* were used as database. All images have resolution of 1024x650 pixels and were taken by an OPTOMAP machine which allowed an approximately 200º fundus image of the retina. The dataset contains images correctly acquired and images containing malfunctions or a strong amount of artifacts. Each fundus image has the normal features of an OPTOMAP image, i.e., information only on red and green channels and each one with 256 intensity levels. No modification, to adapt or improve the images was necessary for the program to work.

5.1.2 Methods

The results evaluation were performed by comparing the resulting image with the original image having the artifacts marked by a specialized person. The assessment was done comparing block by block and one block could fall into one of four testing results: *True Positive (TP)* if the block were *correctly* selected as *part of* the clinical ROI; *True Negative (TN)* if the block were *correctly* selected as *not part of* the clinical ROI; *False Positive (FP)* if a block were *incorrectly* selected as *part of* the clinical ROI; *False Negative (FN)* if a block were *incorrectly* selected as *not part of* the clinical ROI;

For the comparative analysis indicators such as sensitivity, specificity, precision, accuracy and false negative rate were calculated.

Finally, to assess a final error, a cost matrix with weights, were performed to unite the values of false negative error and false positive error into one.

5.1.2.1 Sensitivity, Specificity

In this work, sensitivity represents the proportion of the positives of the image that have been correctly evaluated as such and can be calculated using the formula below.

$$sensitivity = {}^{TP}/_{FN + TP}$$

On the other hand, specificity represents the proportion of the negatives of the image that have been correctly evaluated as such and can be calculated using the formula below.

$$specitivity = {}^{TN}/_{FP + TN}$$

Both specificity and sensitivity can vary between 0 and 100%, where a result close to 0% will stand for a low value and a result close to 100% for a high program.

5.1.2.2 Negative and Positive Predictive Values

The negative predictive value (PPV) represents the amount of tests considered negatives that were in fact true negatives and can be calculated using the following formula.

$$NPV = {}^{TN}/_{FN + TN}$$

The positive predictive value (NPV) represents the amount of tests considered positives that were, in fact, true positives and can be calculated using the following formula.

$$PPV = {}^{TP}/_{FP + TP}$$

In this work, both NPV and PPV, will describe its performance. A result close to 100% of those values will stand for a precise program.

5.1.2.3 Accuracy and Precision

In this work accuracy represents a degree of closeness of the result obtained to the true and known value. It can be calculated using the following formula.

$$accuracy = {}^{TP + TN}/_{P + N}$$

On the other hand, precision represents a degree of closeness of two or more results to each other and can be calculated with the formula below.

$$precision = {}^{TP}/_{FP + TP}$$

A precision result close to 100% will stand for a program which, under the same conditions, will show the same results while a accuracy result close to 100% will stand for a program whose results are very close to the real and expected values. A program is considered valid when both precision and accuracy are close to 100%.

5.2 Results

5.2.1 Sensitivity and Specificity Analysis

The sensitivity and specificity per image were calculated (Figure 5.1) as well the mean for both values (Table 5.1).

Figure 5.1 - Graphics of Sensitivity and Specificity per Image.

Table 5.1 - Mean Sensitivity and Specificity.

	SENSTIIVITY	SPECIFICITY
Mean Value (%)	96,928	99,854

5.2.2 Negative and Positive Predictive Values

The NPV and PPV per image were calculated (Figure 5.2) as well the mean for both values (Table 5.2).

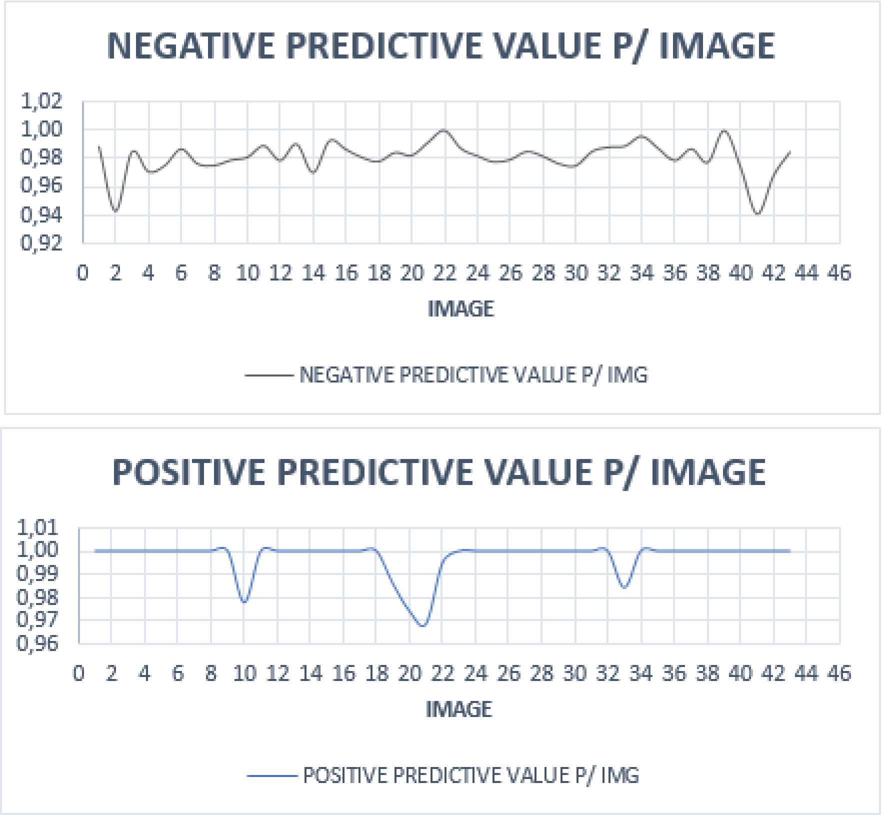

Figure 5.2 - Graphics of NPV and PPV per Image.

Table 5.2 - Mean PPV and NPV.

	POSITIVE PREDICTIVE VALUE	NEGATIVE PREDICTIVE VALUE
Mean Value (%)	99,733	98,121

5.2.3 Accuracy and Precision

The accuracy and precision per image were calculated (Figure 5.3) as well the mean for both values (Table 5.3).

Figure 5.3 - Graphics of Accuracy and Precision per Image.

Table 5.3 - Mean Accuracy and Precision.

	ACCURACY	PRECISION
Mean Value (%)	98,756	99,733

5.2.4 Cost Matrix

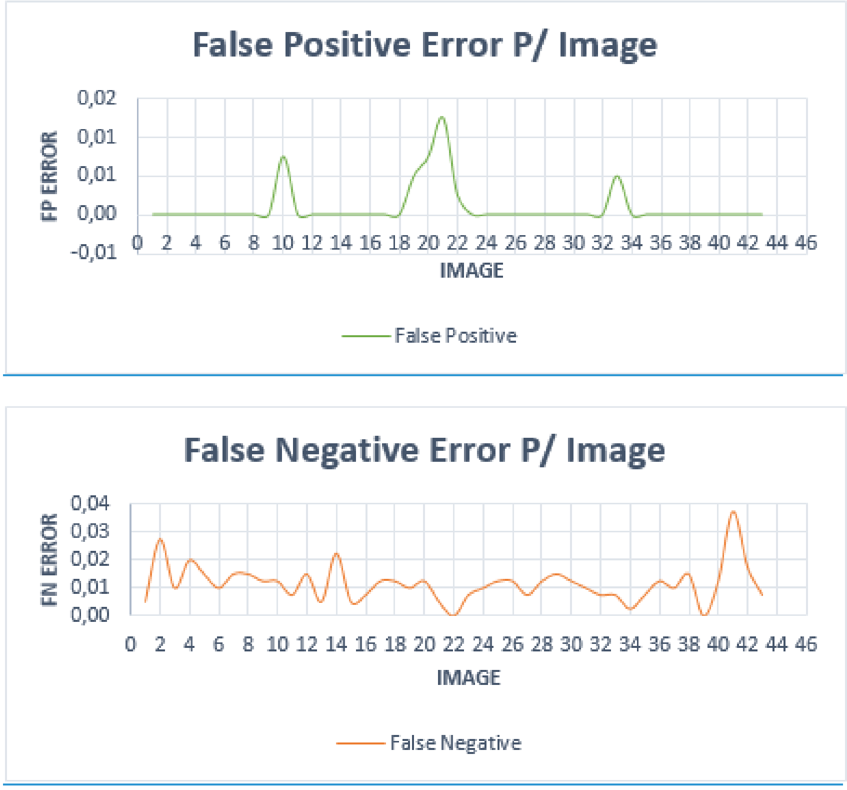

Figure 5.4 - Graphics of FP and FN per image.

Table 5.4 - Mean FP and FN.

	FP	FN
Mean Value (%)	0,0930	1,1512

Table 5.5 - Cost Matrix for FP and FN.

	FN	FP
FN	0	100
FP	40	0

$$final\ error = {}^{(FP\ error * 100) + (FN\ error * 40)}\!\Big/_{100 + 40} = 0{,}3953\%$$

5.3 Summary

This results can be considered good as they validate the automatic delimitation of the clinical ROI in retinal fundus images program.

The program can be considered accurate and precise as the results close to 100% (accuracy - 98,8%, precision - 99,7%) of both values demonstrate, even so the precision values are slightly better than the accuracy values which means that this program, under the same conditions, will present always excellent results that are very similar to the actual ones.

With values of NPV and PPV of 99,7% and 98,1% respectively, the precision assessment can be elaborated as both the "positive values precision" and "negative values precision", PPV and NPV respectively, are very good standing then for a very good precision as well, still it can be said that the program is more precise for positive values as the values demonstrate.

Finally, and more important, assessing the specificity and sensitivity values it can be seen an almost perfect specificity (99,9%), which in this work stands for an almost perfect ability to correctly find the negative zones, zones with artifacts, in the image whereas for the sensitivity the values are slightly worse (96,9%), corresponding then for a slightly worse ability for the program to correctly find positive zones, zones corresponding for the clinical ROI, in the image.

As shown in the cost matrix (Table 5.5) the false positive error, in this case, has more relevance than the false negative error so the final error for this work will more influenced by the false positive error. The final error calculated (0,395%) can be considered low and very satisfactory.

6

Chapter 6. Conclusion

This thesis presented a full methodology for automatic delimitation of the clinical ROI in fundus images of the retina. By using digital imaging processing techniques a user independent program was developed, which allows a more objective criteria for automatic delimitation of the ROI in retinal fundus images.

Ultimately, supplying a tool for automatic disease diagnosis and automatic vessel segmentation programs that can reduce their false positives may prove to be very important. As the clinical ROI area in the resulting image is exactly as the same as that area in the original image, those automatic programs need no previous or extra treatment for them to properly work. Thus, the existence of a tool that can be incorporated into software with the advantage of instantly improve its performance, may reveal to be of great importance.

Having an algorithm that does not require user intervention not only improve its accuracy and repeatability, but also proportionate the use of less human resources and also accelerates the process, which, eventually, end up improving the patients quality of life.

Although there are published works on suppressing eyelashes and/or eyelids, the majority was based on heavy mathematic functions and algorithms which not only are have a slow execution, but also demonstrate results far from expected. Marking those regions containing artifacts based on the image features and obtaining results through an automatic classifier not only show an acceptable timeframe but also improvement on the quality of the results obtained.

To obtain the results a methodology was proposed containing three methods: the image pre-processing phase, the image processing phase and the image post-processing phase. In the first phase all image features required for the next phase are acquired and prepared accordingly. In the next phase the features are put through ANNs and each of them will reproduce a ROI. In the final phase an algorithm for aggregating the ROIs is executed and a single ROI is produced. This single ROI is then post-processed to clean the edges and eliminate misclassified regions from which a final clinical ROI is created.

The methodology was validated with a software created in C# which allowed for a comparison between images to assess its validation.

For the evaluation of the results a statistical analysis was performed. The accuracy, precision, specificity, sensitivity and an estimated final program error have been calculated. From this statistical analysis it was assessed that results were very good in all indicators, validating the proposed methodology.

Although the results seem to be very satisfactory some critical analysis is necessary. The images database of 43 images, despite having a large variety of fundus images, may prove to be short on quality and quantity to represent the full spectrum of possible retinal fundus images. Though the specificity value is very good an improvement on the sensitivity value may prove to be necessary as some regions containing arteries and veins by being falsely selected as containing artifacts became cut out of the image. Notwithstanding the fact that the GUI of the program is simple and efficient, some extra work on improving it can still be done. Also, the algorithms might require some improvements since it is not only the results that are important evaluating a program but also its efficiency, which can always be improved and evolved.

As a conclusion, the automatic delimitation of the clinical region of interest in ultra-wide field of view images of the retina has proven to be reliable and to have a very positive balance since the positives largely overlaps the negatives.

7

Chapter 7. Bibliography

“BRANCH RETINAL ARTERY OCCLUSION.” retinamaine.com/patient-education. Slickfish studios, n.d. Web. 10 Feb. 2014.

“UVEITIS.” retinamaine.com/patient-education. Slickfish studios, n.d. Web. 10 Feb. 2014.

Bachoo, A.K., Tapamo, J.R., 2005. Texture detection for segmentation of iris images. In: Proc. ACM Internat. Conf. on South African Institute of Computer Scientists and Information Technologists, pp. 236–243.

Campbell, John Peter et al. 2012. “Wide-Field Retinal Imaging in the Management of Noninfectious Posterior Uveitis.” *American journal of ophthalmology* 154(5): 908–911.e2. http://www.ncbi.nlm.nih.gov/pubmed/22935598 (February 1, 2014).

Chen, Y. et al., 2006. Localized iris image quality using 2-D wavelets, advances in biometrics. In: Internat. Conf. ICB 2006, Hong Kong, China, pp. 373–381.

Cheng, Sam C K et al. 2008. “Use of the Optomap with Lid Retraction and Its Sensitivity and Specificity.” *Clinical & experimental optometry : journal of the Australian Optometrical Association* 91(4): 373–78. http://www.ncbi.nlm.nih.gov/pubmed/18601667 (November 11, 2013).

Cunha-Vaz, José, Luisa Ribeiro, and Conceição Lobo. 2014. "Phenotypes and Biomarkers of Diabetic Retinopathy." *Progress in retinal and eye research* 41: 90–111. http://www.ncbi.nlm.nih.gov/pubmed/24680929 (August 11, 2014).

Davson, H. (1980). *Physiology of the Eye, Fourth Edition.* New York: Academic Press.

Heaton, Jeff. 2008. 99 *Introduction to Neural Networks with C#*. Second. ed. WordsRU.com. Saint Louis: Heaton Research, Inc.

Hong, Bryan Kun, Hossein Nazari Khanamiri, and Narsing A Rao. 2013. "Role of Ultra-Wide Fi Eld Fl Uorescein Angiography in the Management of Uveitis." *Canadian Journal of Ophthalmology/Journal canadien d'ophtalmologie* 48(6): 489–93. http://dx.doi.org/10.1016/j.jcjo.2013.05.009.

Huang, J., Wang, Y., Cui, J., Tan, T., 2004. Noise removal and impainting model for iris image. In: Proc. IEEE Internat. Conf. on Image Processing, pp. 285–288.

Jang, Young Kyoon, Byung Jun Kang, and Kang Ryoung Park. 2008. "A Study on Eyelid Localization Considering Image Focus for Iris Recognition." *Pattern Recognition Letters* 29(11): 1698–1704. http://linkinghub.elsevier.com/retrieve/pii/S0167865508001578 (January 27, 2014).

Jones, William L. 2004. "Limitations of the Panoramic 200 Optomap." *Optometry and vision science : official publication of the American Academy of Optometry* 81(3): 165–66. http://www.ncbi.nlm.nih.gov/pubmed/15017174.

Kang, B.J., Park, K.R., 2007. A robust eyelash detection based on iris focus assessment. Pattern Recognition Lett. 28 (13), 1630–1639.

Kay, Christine, Elliott Sohn and Michael Abràmoff. "Using Biomarkers for Retinal Disease Risk Assessment and Management." retinalphysician.com/articleviewer.aspx?articleID=105898. Retinal Physician, 1 Jul. 2011. Web. 10 Feb. 2014.

Kernt, Marcus et al. 2012. "Assessment of Diabetic Retinopathy Using Nonmydriatic Ultra-Widefield Scanning Laser Ophthalmoscopy (Optomap) Compared with ETDRS 7-Field Stereo Photography." *Diabetes care* 35(12): 2459–63. http://www.pubmedcentral.nih.gov/articlerender.fcgi?artid=3507573&tool=pmcentrez&rendertype=abstract (February 12, 2014).

Kolb, Helga. “Simple Anatomy of the Retina by Helga Kolb.” webvision.med.utah.edu/book/part-i-foundations/simple-anatomy-of-the-retinaI, Wordpress, 8 Oct. 2011. Web. 10 Feb. 2014.

Lens, A., Nemeth, S. C., & Ledford, J. K. (2008). *Ocular Anatomy and Physiology.* New Jersey: SLACK Incorporated.

Li, Peihua, Xiaomin Liu, Lijuan Xiao, and Qi Song. 2010. “Robust and Accurate Iris Segmentation in Very Noisy Iris Images.” *Image and Vision Computing* 28(2): 246–53. http://linkinghub.elsevier.com/retrieve/pii/S0262885609000754 (January 27, 2014).

Liu, X. et al., 2005. Experiments with an improved iris segmentation algorithm. In: 4th IEEE Workshop on Automatic Identification Advanced Technologies (AutoID’05), New York, USA, pp. 118–123.

Maenpaa, T., 2005. An iterative algorithm for fast iris detection, advances in biometric per-son authentication. In: Internat. Wokshop on Biometric Recognition Systems, IWBRS 2005, Beijing, China, pp. 127–134.

Manivannan, Ayyakkannu et al. 2005. 140 American Journal of Ophthalmology *Ultra-Wide-Field Fluorescein Angiography of the Ocular Fundus*. http://www.sciencedirect.com/science/article/pii/S0002939405002795 (November 11, 2013).

Masek, L., 2003. Recognition of Human Iris Patterns for Biometric Identification, Bachelors Thesis, University of Western Australia.

McIntosh RL, Mohamed Q, Saw SM, Wong TY. Interventions for branch retinal vein occlusion: an evidence-based system- atic review. Ophthalmology 2007;114:835–46.

Min, Tae-Hong, and Rae-Hong Park. 2009. “Eyelid and Eyelash Detection Method in the Normalized Iris Image Using the Parabolic Hough Model and Otsu’s Thresholding Method.” *Pattern Recognition Letters* 30(12): 1138–43. http://linkinghub.elsevier.com/retrieve/pii/S0167865509000683 (January 27, 2014).

Neubauer, Aljoscha S et al. 2008. “Nonmydriatic Screening for Diabetic Retinopathy by Ultra-Widefield Scanning Laser Ophthalmoscopy (Optomap).” *Graefe’s archive for clinical and experimental ophthalmology = Albrecht von Graefes Archiv für klinische und experimentelle Ophthalmologie*

246(2): 229–35. http://www.ncbi.nlm.nih.gov/pubmed/17622548 (February 12, 2014).

Niemeijer, Meindert et al. 2007. "Automated Detection and Differentiation of Drusen, Exudates, and Cotton-Wool Spots in Digital Color Fundus Photographs for Diabetic Retinopathy Diagnosis." *Investigative ophthalmology & visual science* 48(5): 2260–67. http://www.pubmedcentral.nih.gov/articlerender.fcgi?artid=2739583&tool=pmcentrez&rendertype=abstract (September 9, 2014).

Ortiz-rivera, Vanessa, Charles V Stewart, Delia Cabrera, and Badrinath Roysam. 2007. "Suppression of the Eyelash Artifact in Ultra- Widefield Retinal Images." In *2007 Thrust R2B Localized Probing and Mosaicing Methods Conference*, , 38. http://hdl.handle.net/2047/d10008883.

Otsu, Nobuyuki. 1975. "A Tlreshold Selection Method from Gray-Level Histograms." *Automatica* 11: 285–96.

Patel, Ravi D et al. 2013. "Characterization of Ischemic Index Using Ultra-Widefield Fluorescein Angiography in Patients with Focal and Diffuse Recalcitrant Diabetic Macular Edema." *American journal of ophthalmology* 155(6): 1038–1044.e2. http://www.ncbi.nlm.nih.gov/pubmed/23453693 (January 23, 2014).

Perez-Rovira, A, K Zutis, J P Hubschman, and E Trucco. 2011. "Improving Vessel Segmentation in Ultra-Wide Field-of-View Retinal Fluorescein Angiograms." *Conference proceedings : ... Annual International Conference of the IEEE Engineering in Medicine and Biology Society. IEEE Engineering in Medicine and Biology Society. Conference* 2011: 2614–17. http://www.ncbi.nlm.nih.gov/pubmed/22254877 (November 11, 2013).

Prasad, Pradeep S et al. 2010. "Ultra Wide-Field Angiographic Characteristics of Branch Retinal and Hemicentral Retinal Vein Occlusion." *Ophthalmology* 117(4): 780–84. http://www.ncbi.nlm.nih.gov/pubmed/20045570 (February 1, 2014).

Silva, Paolo S. et al. 2013. "Peripheral Lesions Identified by Mydriatic Ultrawide Field Imaging: Distribution and Potential Impact on Diabetic Retinopathy Severity." *Ophthalmology*. http://www.sciencedirect.com/science/article/pii/S0161642013004132 (November 11, 2013).

Tsui, Irena et al. 2013. “Peripheral Fluorescein Angiographic Findings in Fellow Eyes of Patients with Branch Retinal Vein Occlusion.” 2013.

Vezhnevets, V. et al., 2003. Robust and accurate eye contour extraction. In: Proc. Graphicon –2003, Moscow, Russia, pp. 81–84.

Wessel MM, Aaker GD, Parlitsis G, et al. Ultra-wide-field angiography improves the detection and classification of dia- betic retinopathy. Retina 2012;32:785–91.

Wilson, P. J., Ellis, J. D., MacEwen, C. J., Ellingford, A., Talbot, J., & Leese, G. P. (2010). Screening for diabetic retinopathy: a comparative trial of photography and scanning laser ophthalmoscopy. Ophthalmologica. Journal International D’ophtalmologie. International Journal of Ophthalmology. Zeitschrift Für Augenheilkunde, 224(4), 251–7. doi:10.1159/000284351

Zhang, D., Monro, D.M., Rakshit, S., 2006. Eyelash removal method for human iris recognition. In: Proc. IEEE Internat. Conf. on Image Processing, pp. 285–288.

Zutis, K., Trucco, E., Hubschman, J. P., Reed, D., Shah, S., & van Hemert, J. (2013). Towards automatic detection of abnormal retinal capillaries in ultra-widefield-of-view retinal angiographic exams. Conference Proceedings : ... Annual International Conference of the IEEE Engineering in Medicine and Biology Society. IEEE Engineering in Medicine and Biology Society. Conference, 2013, 7372–5. Retrieved from http://www.ncbi.nlm.nih.gov/pubmed/24111448

Annex A

In this Annex A, all the results will be shown.

Table 7.1 - First Data comparing results according to the number of blocks cropped from the image for the green channel and magnitude FFT characteristics.

ERROR	IMG	GREEN			MAGNITUDE		
		PIXEL					
		LOW	NORMAL	HIGH	LOW	NORMAL	HIGH
FN	IMG1	0,0370	0,0700	0,0833	0,2840	0,4700	0,4306
FP		0,0864	0,0800	0,0625	0,0000	0,0000	0,0000
TOTAL		0,1235	0,1500	0,1458	0,2840	0,4700	0,4306
FN	IMG2	0,1358	0,1700	0,1458	0,6667	0,7400	0,7639
FP		0,0123	0,0100	0,0139	0,0000	0,0000	0,0000
TOTAL		0,1481	0,1800	0,1597	0,6667	0,7400	0,7639
FN	IMG3	0,0370	0,0600	0,0625	0,1235	0,2300	0,1597
FP		0,0741	0,0400	0,0347	0,0123	0,0000	0,0000
TOTAL		0,1111	0,1000	0,0972	0,1358	0,2300	0,1597
FN	IMG4	0,0864	0,1000	0,1042	0,2222	0,3300	0,3056
FP		0,0988	0,0700	0,0694	0,0370	0,0100	0,0069
TOTAL		0,1852	0,1700	0,1736	0,2593	0,3400	0,3125
FN	IMG5	0,0494	0,0400	0,0764	0,2222	0,3500	0,3125
FP		0,0741	0,0300	0,0486	0,0370	0,0200	0,0139
TOTAL		0,1235	0,0700	0,1250	0,2593	0,3700	0,3264
FN	IMG6	0,0988	0,0900	0,1458	0,1481	0,2400	0,2153
FP		0,0741	0,0600	0,0625	0,0741	0,0300	0,0417
TOTAL		0,1728	0,1500	0,2083	0,2222	0,2700	0,2569
FN	IMG7	0,0741	0,0900	0,0833	0,3457	0,3125	0,4236
FP		0,0864	0,1000	0,0625	0,0123	0,0000	0,0000
TOTAL		0,1605	0,1900	0,1458	0,3580	0,3125	0,4236
FN	IMG8	0,1111	0,1100	0,1181	0,2346	0,3000	0,2778
FP		0,0370	0,0300	0,0208	0,0247	0,0200	0,0139
TOTAL		0,1481	0,1400	0,1389	0,2593	0,3200	0,2917

FN	IMG9	0,0741	0,0800	0,1111	0,2469	0,3200	0,3056
FP		0,0370	0,0300	0,0139	0,0000	0,0000	0,0000
TOTAL		0,1111	0,1100	0,1250	0,2469	0,3200	0,3056
FN	IMG10	0,0494	0,0400	0,0556	0,1852	0,2800	0,2083
FP		0,0741	0,0900	0,0764	0,0247	0,0000	0,0000
TOTAL		0,1235	0,1300	0,1319	0,2099	0,2800	0,2083
FN	IMG11	0,0988	0,1100	0,1389	0,1481	0,3000	0,2431
FP		0,0123	0,0100	0,0069	0,0247	0,0200	0,0139
TOTAL		0,1111	0,1200	0,1458	0,1728	0,3200	0,2569
FN	IMG12	0,0000	0,0000	0,0000	0,0247	0,0900	0,0556
FP		0,1235	0,1000	0,0903	0,0494	0,0100	0,0069
TOTAL		0,1235	0,1000	0,0903	0,0741	0,1000	0,0625
FN	IMG13	0,0864	0,0700	0,1042	0,2222	0,3200	0,2639
FP		0,0247	0,0100	0,0139	0,0247	0,0100	0,0069
TOTAL		0,1111	0,0800	0,1181	0,2469	0,3300	0,2708
FN	IMG14	0,0370	0,0700	0,0556	0,1728	0,1900	0,1806
FP		0,0370	0,0200	0,0208	0,0247	0,0200	0,0139
TOTAL		0,0741	0,0900	0,0764	0,1975	0,2100	0,1944
FN	IMG16	0,0370	0,0500	0,0625	0,1111	0,1800	0,1528
FP		0,1235	0,1200	0,1042	0,0741	0,0200	0,0417
TOTAL		0,1605	0,1700	0,1667	0,1852	0,2000	0,1944
FN	IMG17	0,0370	0,0200	0,0486	0,1975	0,2800	0,2569
FP		0,0864	0,0700	0,0347	0,0247	0,0100	0,0069
TOTAL		0,1235	0,0900	0,0833	0,2222	0,2900	0,2639
FN	IMG19	0,0370	0,0500	0,0556	0,1728	0,2400	0,2083
FP		0,1358	0,1100	0,1042	0,0494	0,0100	0,0139
TOTAL		0,1728	0,1600	0,1597	0,2222	0,2500	0,2222
FN	IMG20	0,0741	0,0900	0,1181	0,1852	0,3000	0,2361
FP		0,0617	0,0200	0,0208	0,0247	0,0200	0,0069
TOTAL		0,1358	0,1100	0,1389	0,2099	0,3200	0,2431
FN	IMG21	0,0370	0,0300	0,0417	0,1605	0,2100	0,1875
FP		0,0617	0,0600	0,0417	0,0247	0,0200	0,0069
TOTAL		0,0988	0,0900	0,0833	0,1852	0,2300	0,1944
FN	IMG22	0,0370	0,0400	0,0486	0,0741	0,1000	0,0625
FP		0,0864	0,0500	0,0417	0,0864	0,0500	0,0347
TOTAL		0,1235	0,0900	0,0903	0,1605	0,1500	0,0972
FN	IMG23	0,0370	0,0600	0,0625	0,1728	0,2400	0,1736
FP		0,0617	0,0600	0,0417	0,0370	0,0100	0,0200
TOTAL		0,0988	0,1200	0,1042	0,2099	0,2500	0,1936
FN	IMG24	0,0247	0,0200	0,0278	0,1235	0,2500	0,2222
FP		0,0741	0,0300	0,0278	0,0247	0,0100	0,0069
TOTAL		0,0988	0,0500	0,0556	0,1481	0,2600	0,2292

FN	IMG25	0,0123	0,0100	0,0208	0,0370	0,1900	0,1181
FP		0,0494	0,0300	0,0347	0,0247	0,0100	0,0069
TOTAL		0,0617	0,0400	0,0556	0,0617	0,2000	0,1250
FN	IMG26	0,0123	0,0300	0,0278	0,1111	0,2300	0,1458
FP		0,0864	0,0500	0,0417	0,0247	0,0100	0,0069
TOTAL		0,0988	0,0800	0,0694	0,1358	0,2400	0,1528
FN	IMG27	0,0123	0,0200	0,0278	0,0864	0,1800	0,0972
FP		0,0000	0,0200	0,0278	0,0247	0,0100	0,0069
TOTAL		0,0123	0,0400	0,0556	0,1111	0,1900	0,1042
FN	IMG28	0,0247	0,0200	0,0208	0,1358	0,2900	0,1736
FP		0,0617	0,0300	0,0417	0,0494	0,0200	0,0069
TOTAL		0,0864	0,0500	0,0625	0,1852	0,3100	0,1806
FN	IMG29	0,0123	0,0100	0,0347	0,1975	0,2900	0,2569
FP		0,1358	0,1100	0,0556	0,0247	0,0100	0,0069
TOTAL		0,1481	0,1200	0,0903	0,2222	0,3000	0,2639
FN	IMG30	0,0247	0,0200	0,0278	0,0617	0,1000	0,0625
FP		0,0617	0,0600	0,0347	0,0370	0,0200	0,0139
TOTAL		0,0864	0,0800	0,0625	0,0988	0,1200	0,0764
FN	IMG31	0,0247	0,0300	0,0278	0,1235	0,2000	0,1667
FP		0,0988	0,1000	0,0972	0,0247	0,0100	0,0139
TOTAL		0,1235	0,1300	0,1250	0,1481	0,2100	0,1806
FN	IMG32	0,0247	0,0800	0,0486	0,2099	0,2500	0,2083
FP		0,0247	0,0400	0,0139	0,0247	0,0200	0,0069
TOTAL		0,0494	0,1200	0,0625	0,2346	0,2700	0,2153
FN	IMG33	0,0000	0,0000	0,0000	0,0988	0,1800	0,1042
FP		0,2099	0,1900	0,1667	0,0864	0,0300	0,0417
TOTAL		0,2099	0,1900	0,1667	0,1852	0,2100	0,1458
FN	IMG34	0,0000	0,0000	0,0000	0,1358	0,2300	0,1319
FP		0,1605	0,1600	0,1181	0,0123	0,0000	0,0000
TOTAL		0,1605	0,1600	0,1181	0,1481	0,2300	0,1319
FN	IMG35	0,0864	0,0800	0,1181	0,1358	0,2000	0,1667
FP		0,0494	0,0400	0,0347	0,0370	0,0100	0,0139
TOTAL		0,1358	0,1200	0,1528	0,1728	0,2100	0,1806
FN	IMG36	0,0617	0,0200	0,0347	0,1358	0,2300	0,1736
FP		0,0864	0,0700	0,0486	0,0247	0,0100	0,0069
TOTAL		0,1481	0,0900	0,0833	0,1605	0,2400	0,1806
FN	IMG37	0,1111	0,1000	0,1250	0,1605	0,3100	0,2083
FP		0,0370	0,0400	0,0139	0,0370	0,0200	0,0069
TOTAL		0,1481	0,1400	0,1389	0,1975	0,3300	0,2153
FN	IMG38	0,0247	0,0000	0,0278	0,2469	0,3400	0,2361
FP		0,0617	0,0400	0,0139	0,0247	0,0100	0,0069
TOTAL		0,0864	0,0400	0,0417	0,2716	0,3500	0,2431

FN		0,0247	0,0200	0,0278	0,1605	0,2400	0,1944
FP	IMG39	0,0864	0,0700	0,0625	0,0123	0,0000	0,0000
TOTAL		0,1111	0,0900	0,0903	0,1728	0,2400	0,1944
FN		0,0000	0,0000	0,0000	0,1111	0,1800	0,1111
FP	IMG40	0,1358	0,1000	0,0972	0,0247	0,0000	0,0139
TOTAL		0,1358	0,1000	0,0972	0,1358	0,1800	0,1250
FN		0,0000	0,0000	0,0069	0,2593	0,4200	0,2708
FP	IMG42	0,0617	0,0500	0,0278	0,0000	0,0000	0,0000
TOTAL		0,0617	0,0500	0,0347	0,2593	0,4200	0,2708
FN		0,0123	0,0100	0,0139	0,1358	0,2900	0,1458
FP	IMG43	0,0370	0,0400	0,0208	0,0000	0,0000	0,0000
TOTAL		0,0494	0,0500	0,0347	0,1358	0,2900	0,1458
FN		0,0000	0,0000	0,0139	0,1728	0,3300	0,1250
FP	IMG44	0,0247	0,0200	0,0139	0,0000	0,0000	0,0000
TOTAL		0,0247	0,0200	0,0278	0,1728	0,3300	0,1250
FN		0,0000	0,0000	0,0000	0,0617	0,3400	0,1667
FP	IMG46	0,0864	0,0800	0,0833	0,0123	0,0000	0,0000
TOTAL		0,0864	0,0800	0,0833	0,0741	0,3400	0,1667
Total error p/ ANN		0,1158	0,1060	0,1052	0,2005	0,2803	0,2220
Total error p/ ANN (%)		11,581	10,595	10,516	20,047	28,030	22,204
False Negative error p/ ANN		0,0420	0,0455	0,0561	0,1720	0,2689	0,2121
False Negative error p/ ANN (%)		4,203	4,548	5,605	17,196	26,887	21,214
False Positive error p/ ANN		0,0738	0,0605	0,0491	0,0285	0,0114	0,0099
False Negative error p/ ANN (%)		7,378	6,048	4,911	2,851	1,143	0,990

Table 7.2 - First Data comparing results according to the number of blocks cropped from the image for the red channel characteristics.

ERROR	IMG	RED					
		PIXEL			LOW VALUE		
		LOW	NORMAL	HIGH	LOW	NORMAL	HIGH
FN	IMG1	0,1481	0,2500	0,2569	0,2222	0,2400	0,2361
FP		0,0000	0,0000	0,0000	0,0000	0,0000	0,0000
TOTAL		0,1481	0,2500	0,2569	0,2222	0,2400	0,2361
FN	IMG2	0,4074	0,4400	0,4236	0,3086	0,3000	0,3194
FP		0,0000	0,0000	0,0000	0,0000	0,0000	0,0000
TOTAL		0,4074	0,4400	0,4236	0,3086	0,3000	0,3194
FN	IMG3	0,1235	0,1100	0,1319	0,1235	0,1000	0,1111
FP		0,0000	0,0100	0,0000	0,0000	0,0000	0,0000
TOTAL		0,1235	0,1200	0,1319	0,1235	0,1000	0,1111
FN	IMG4	0,1358	0,12	0,1667	0,1358	0,13	0,1528
FP		0,0370	0,02	0,0139	0,0247	0,0100	0,0139
TOTAL		0,1728	0,1400	0,1806	0,1605	0,1400	0,1667
FN	IMG5	0,1975	0,1800	0,2153	0,1728	0,1600	0,1944
FP		0,0247	0,0100	0,0069	0,0000	0,0000	0,0000
TOTAL		0,2222	0,1900	0,2222	0,1728	0,1600	0,1944
FN	IMG6	0,0617	0,1100	0,1111	0,1111	0,1200	0,1111
FP		0,0741	0,0700	0,0764	0,0617	0,0700	0,0556
TOTAL		0,1358	0,1800	0,1875	0,1728	0,1900	0,1667
FN	IMG7	0,2840	0,2900	0,3403	0,2593	0,2700	0,3056
FP		0,0000	0,0000	0,0000	0,0000	0,0000	0,0000
TOTAL		0,2840	0,2900	0,3403	0,2593	0,2700	0,3056
FN	IMG8	0,1605	0,1700	0,1736	0,1728	0,1600	0,1806
FP		0,0247	0,0100	0,0000	0,0000	0,0000	0,0000
TOTAL		0,1852	0,1800	0,1736	0,1728	0,1600	0,1806
FN	IMG9	0,1852	0,1700	0,1944	0,1605	0,1900	0,1944
FP		0,0000	0,0000	0,0069	0,0000	0,0000	0,0000
TOTAL		0,1852	0,1700	0,2014	0,1605	0,1900	0,1944
FN	IMG10	0,1358	0,1300	0,1736	0,1481	0,1300	0,1319
FP		0,0123	0,0200	0,0208	0,0123	0,0100	0,0139
TOTAL		0,1481	0,1500	0,1944	0,1605	0,1400	0,1458
FN	IMG11	0,1111	0,1100	0,1319	0,1481	0,1400	0,1319
FP		0,0000	0,0000	0,0000	0,0000	0,0000	0,0000
TOTAL		0,1111	0,1100	0,1319	0,1481	0,1400	0,1319
FN	IMG12	0,0247	0,0500	0,0417	0,0247	0,0300	0,0417
FP		0,0370	0,0200	0,0139	0,0123	0,0200	0,0139
TOTAL		0,0617	0,0700	0,0556	0,0370	0,0500	0,0556
FN	IMG13	0,1235	0,1100	0,1458	0,1235	0,1000	0,1181
FP		0,0494	0,0400	0,0069	0,0123	0,0200	0,0069

TOTAL		0,1728	0,1500	0,1528	0,1358	0,1200	0,1250
FN		0,1975	0,1900	0,1806	0,1852	0,2100	0,1875
FP	IMG14	0,0247	0,0100	0,0139	0,0000	0,0000	0,0069
TOTAL		0,2222	0,2000	0,1944	0,1852	0,2100	0,1944
FN		0,0741	0,0900	0,0903	0,0741	0,0900	0,0903
FP	IMG16	0,0370	0,0500	0,0625	0,0494	0,0300	0,0208
TOTAL		0,1111	0,1400	0,1528	0,1235	0,1200	0,1111
FN		0,1111	0,1100	0,1319	0,1111	0,1100	0,1389
FP	IMG17	0,0247	0,0100	0,0139	0,0123	0,0100	0,0139
TOTAL		0,1358	0,1200	0,1458	0,1235	0,1200	0,1528
FN		0,1111	0,1200	0,1528	0,1235	0,1300	0,1250
FP	IMG19	0,0494	0,0400	0,0486	0,0370	0,0200	0,0347
TOTAL		0,1605	0,1600	0,2014	0,1605	0,1500	0,1597
FN		0,0988	0,1200	0,1319	0,1111	0,1100	0,1250
FP	IMG20	0,0123	0,0300	0,0069	0,0123	0,0000	0,0069
TOTAL		0,1111	0,1500	0,1389	0,1235	0,1100	0,1319
FN		0,0988	0,1000	0,1181	0,0864	0,1000	0,1042
FP	IMG21	0,0370	0,0400	0,0208	0,0123	0,0000	0,0069
TOTAL		0,1358	0,1400	0,1389	0,0988	0,1000	0,1111
FN		0,0370	0,0500	0,0625	0,0617	0,0600	0,0556
FP	IMG22	0,0617	0,0600	0,0694	0,0370	0,0300	0,0278
TOTAL		0,0988	0,1100	0,1319	0,0988	0,0900	0,0833
FN		0,0741	0,0800	0,0764	0,0864	0,0800	0,0625
FP	IMG23	0,0617	0,0500	0,0347	0,0123	0,0100	0,0139
TOTAL		0,1358	0,1300	0,1111	0,0988	0,0900	0,0764
FN		0,0370	0,0300	0,0347	0,0123	0,0300	0,0208
FP	IMG24	0,0000	0,0100	0,0139	0,0123	0,0100	0,0139
TOTAL		0,0370	0,0400	0,0486	0,0247	0,0400	0,0347
FN		0,0247	0,0200	0,0417	0,0000	0,0300	0,0139
FP	IMG25	0,0000	0,0000	0,0000	0,0000	0,0000	0,0000
TOTAL		0,0247	0,0200	0,0417	0,0000	0,0300	0,0139
FN		0,0494	0,0600	0,0625	0,0494	0,0600	0,0556
FP	IMG26	0,0000	0,0000	0,0000	0,0000	0,0100	0,0000
TOTAL		0,0494	0,0600	0,0625	0,0494	0,0700	0,0556
FN		0,0370	0,0600	0,0347	0,0370	0,0400	0,0347
FP	IMG27	0,0000	0,0100	0,0000	0,0000	0,0000	0,0000
TOTAL		0,0370	0,0700	0,0347	0,0370	0,0400	0,0347
FN		0,1111	0,0800	0,0903	0,0864	0,0800	0,0694
FP	IMG28	0,0000	0,0100	0,0069	0,0000	0,0100	0,0069
TOTAL		0,1111	0,0900	0,0972	0,0864	0,0900	0,0764
FN	IMG29	0,0988	0,1100	0,1111	0,1111	0,1000	0,0764
FP		0,0123	0,0100	0,0069	0,0123	0,0100	0,0000

TOTAL		0,1111	0,1200	0,1181	0,1235	0,1100	0,0764
FN		0,0370	0,0400	0,0417	0,0370	0,0400	0,0347
FP	IMG30	0,0494	0,0600	0,0417	0,0123	0,0200	0,0139
TOTAL		0,0864	0,1000	0,0833	0,0494	0,0600	0,0486
FN		0,0741	0,0700	0,0556	0,0617	0,0600	0,0625
FP	IMG31	0,0741	0,0200	0,0278	0,0123	0,0200	0,0139
TOTAL		0,1481	0,0900	0,0833	0,0741	0,0800	0,0764
FN		0,0741	0,0800	0,0625	0,0494	0,0400	0,0278
FP	IMG32	0,0123	0,0100	0,0000	0,0000	0,0000	0,0000
TOTAL		0,0864	0,0900	0,0625	0,0494	0,0400	0,0278
FN		0,0617	0,0800	0,0764	0,0864	0,0700	0,0833
FP	IMG33	0,0000	0,0000	0,0000	0,0000	0,0000	0,0000
TOTAL		0,0617	0,0800	0,0764	0,0864	0,0700	0,0833
FN		0,1235	0,1300	0,1111	0,1111	0,1300	0,0972
FP	IMG34	0,0123	0,0200	0,0069	0,0000	0,0000	0,0000
TOTAL		0,1358	0,1500	0,1181	0,1111	0,1300	0,0972
FN		0,0617	0,0800	0,0764	0,0741	0,0700	0,0625
FP	IMG35	0,0617	0,0400	0,0278	0,0000	0,0100	0,0069
TOTAL		0,1235	0,1200	0,1042	0,0741	0,0800	0,0694
FN		0,0864	0,0900	0,1042	0,0864	0,1200	0,1042
FP	IMG36	0,0247	0,0400	0,0139	0,0247	0,0100	0,0069
TOTAL		0,1111	0,1300	0,1181	0,1111	0,1300	0,1111
FN		0,0617	0,0700	0,0903	0,0988	0,0900	0,0903
FP	IMG37	0,0494	0,0200	0,0208	0,0000	0,0000	0,0000
TOTAL		0,1111	0,0900	0,1111	0,0988	0,0900	0,0903
FN		0,1358	0,1200	0,1458	0,1358	0,1300	0,1319
FP	IMG38	0,0000	0,0000	0,0000	0,0000	0,0000	0,0000
TOTAL		0,1358	0,1200	0,1458	0,1358	0,1300	0,1319
FN		0,1481	0,1300	0,1389	0,0988	0,1100	0,1319
FP	IMG39	0,0000	0,0000	0,0000	0,0000	0,0000	0,0000
TOTAL		0,1481	0,1300	0,1389	0,0988	0,1100	0,1319
FN		0,0741	0,0700	0,0556	0,0247	0,0600	0,0556
FP	IMG40	0,0370	0,0100	0,0208	0,0247	0,0200	0,0278
TOTAL		0,1111	0,0800	0,0764	0,0494	0,0800	0,0833
FN		0,0864	0,0800	0,0833	0,0247	0,0100	0,0417
FP	IMG42	0,0000	0,0000	0,0000	0,0000	0,0000	0,0000
TOTAL		0,0864	0,0800	0,0833	0,0247	0,0100	0,0417
FN		0,0864	0,0900	0,1042	0,0617	0,0600	0,0625
FP	IMG43	0,0123	0,0100	0,0139	0,0247	0,0200	0,0208
TOTAL		0,0988	0,1000	0,1181	0,0864	0,0800	0,0833
FN	IMG44	0,1235	0,1100	0,0833	0,0617	0,0800	0,0625
FP		0,0123	0,0000	0,0139	0,0247	0,0200	0,0208

TOTAL		0,1358	0,1100	0,0972	0,0864	0,1000	0,0833
FN	IMG46	0,0000	0,0000	0,0000	0,0000	0,0000	0,0000
FP		0,0864	0,0600	0,0347	0,0370	0,0300	0,0278
TOTAL		0,0864	0,0600	0,0347	0,0370	0,0300	0,0278
Total error p/ ANN		0,1311	0,1314	0,1362	0,1129	0,1140	0,1151
Total error p/ ANN (%)		13,110	13,143	13,624	11,287	11,405	11,508
False Negative error p/ ANN		0,1070	0,1119	0,1204	0,1014	0,1040	0,1057
False Negative error p/ ANN (%)		10,700	11,190	12,037	10,141	10,405	10,565
False Positive error p/ ANN		0,0241	0,0195	0,0159	0,0115	0,0100	0,0094
False Negative error p/ ANN (%)		2,410	1,952	1,587	1,146	1,000	0,942

Table 7.3 - False Positive and False Negative error per image before setting the better number of blocks.

Error p/ Image	Error p/ Image (%)	
0,1530	15,30	FN
0,0193	1,93	FP
0,1724	17,24	TOTAL
0,2595	25,95	FN
0,0082	0,82	FP
0,2677	26,77	TOTAL
0,0997	9,97	FN
0,0219	2,19	FP
0,1216	12,16	TOTAL
0,1177	11,77	FN
0,0812	8,12	FP
0,1989	19,89	TOTAL

0,1537	15,37	FN
0,0403	4,03	FP
0,1940	19,40	TOTAL
0,0817	8,17	FN
0,1475	14,75	FP
0,2291	22,91	TOTAL
0,1985	19,85	FN
0,0325	3,25	FP
0,2310	23,10	TOTAL
0,1376	13,76	FN
0,0331	3,31	FP
0,1707	17,07	TOTAL
0,1392	13,92	FN
0,0434	4,34	FP
0,1826	18,26	TOTAL
0,0989	9,89	FN
0,0601	6,01	FP
0,1590	15,90	TOTAL
0,1146	11,46	FN
0,0144	1,44	FP
0,1291	12,91	TOTAL
0,0319	3,19	FN
0,0628	6,28	FP
0,0947	9,47	TOTAL
0,0984	9,84	FN
0,0706	7,06	FP
0,1691	16,91	TOTAL
0,1531	15,31	FN
0,0168	1,68	FP
0,1699	16,99	TOTAL
0,0586	5,86	FN
0,0806	8,06	FP
0,1392	13,92	TOTAL
0,0890	8,90	FN
0,0622	6,22	FP
0,1512	15,12	TOTAL
0,0976	9,76	FN
0,0807	8,07	FP
0,1783	17,83	TOTAL
0,0998	9,98	FN
0,0451	4,51	FP
0,1449	14,49	TOTAL

0,0846	8,46	FN
0,0824	8,24	FP
0,1670	16,70	TOTAL
0,0426	4,26	FN
0,0786	7,86	FP
0,1211	12,11	TOTAL
0,0692	6,92	FN
0,0473	4,73	FP
0,1165	11,65	TOTAL
0,0417	4,17	FN
0,0543	5,43	FP
0,0960	9,60	TOTAL
0,0298	2,98	FN
0,0348	3,48	FP
0,0647	6,47	TOTAL
0,0552	5,52	FN
0,0423	4,23	FP
0,0975	9,75	TOTAL
0,0458	4,58	FN
0,0253	2,53	FP
0,0711	7,11	TOTAL
0,0824	8,24	FN
0,0313	3,13	FP
0,1137	11,37	TOTAL
0,0914	9,14	FN
0,0638	6,38	FP
0,1552	15,52	TOTAL
0,0314	3,14	FN
0,0694	6,94	FP
0,1008	10,08	TOTAL
0,0601	6,01	FN
0,0635	6,35	FP
0,1236	12,36	TOTAL
0,0630	6,30	FN
0,0285	2,85	FP
0,0915	9,15	TOTAL
0,0573	5,73	FN
0,0696	6,96	FP
0,1269	12,69	TOTAL
0,0879	8,79	FN
0,0606	6,06	FP
0,1484	14,84	TOTAL

0,0601	6,01	FN
0,0488	4,88	FP
0,1089	10,89	TOTAL
0,0756	7,56	FN
0,0694	6,94	FP
0,1449	14,49	TOTAL
0,0806	8,06	FN
0,0383	3,83	FP
0,1189	11,89	TOTAL
0,1078	10,78	FN
0,0227	2,27	FP
0,1306	13,06	TOTAL
0,0900	9,00	FN
0,0399	3,99	FP
0,1300	13,00	TOTAL
0,0450	4,50	FN
0,0704	7,04	FP
0,1154	11,54	TOTAL
0,0751	7,51	FN
0,0353	3,53	FP
0,1105	11,05	TOTAL
0,0607	6,07	FN
0,0421	4,21	FP
0,1028	10,28	TOTAL
0,0750	7,50	FN
0,0391	3,91	FP
0,1140	11,40	TOTAL
0,0277	2,77	FN
0,1312	13,12	FP
0,1589	15,89	TOTAL

Table 7.4 - Data of green channel and magnitude FFT before contrast and brightness correction.

IMG	ERROR			
	GREEN		MAGNITUDE	
	PIXEL			
	Extremely High	225	Extremely High	225
	FP	FN	FP	FN
IMG1	0,0133	0,0000	0,0000	0,0756

IMG2	0,0000	0,0178	0,0000	0,1467
IMG3	0,0489	0,0089	0,0000	0,0489
IMG4	0,0133	0,0133	0,0044	0,0711
IMG5	0,0356	0,0089	0,0000	0,0756
IMG7	0,0044	0,0044	0,0000	0,0889
IMG8	0,0222	0,0222	0,0000	0,0800
IMG9	0,0000	0,0044	0,0000	0,0800
IMG10	0,0756	0,0133	0,0000	0,0978
IMG11	0,0000	0,0178	0,0000	0,0489
IMG12	0,0489	0,0044	0,0000	0,0578
IMG13	0,0089	0,0222	0,0000	0,0667
IMG16	0,0756	0,0044	0,0222	0,0178
IMG17	0,0133	0,0044	0,0000	0,0756
IMG19	0,0844	0,0089	0,0000	0,0711
IMG20	0,0089	0,0133	0,0000	0,0667
IMG21	0,0222	0,0044	0,0000	0,0711
IMG22	0,0089	0,0089	0,0044	0,0533
IMG23	0,0311	0,0089	0,0000	0,0800
IMG24	0,0089	0,0000	0,0000	0,0267
IMG25	0,0133	0,0089	0,0000	0,0622
IMG26	0,0133	0,0133	0,0000	0,1200
IMG27	0,0000	0,0089	0,0000	0,1022
IMG28	0,0311	0,0000	0,0000	0,1111
IMG29	0,0267	0,0000	0,0000	0,1156
IMG30	0,0044	0,0133	0,0000	0,0578
IMG31	0,0533	0,0044	0,0000	0,0844
IMG32	0,0000	0,0000	0,0000	0,0444
IMG33	0,0889	0,0000	0,0000	0,0356
IMG34	0,0444	0,0000	0,0000	0,0356
IMG35	0,0267	0,0178	0,0000	0,0711
IMG36	0,0311	0,0000	0,0000	0,0311
IMG37	0,0000	0,0489	0,0000	0,1067
IMG38	0,0133	0,0000	0,0000	0,0756
IMG39	0,0311	0,0044	0,0000	0,0711
IMG40	0,0356	0,0000	0,0000	0,0667
IMG42	0,0000	0,0000	0,0000	0,1511
IMG43	0,0000	0,0178	0,0000	0,1289
IMG44	0,0000	0,0133	0,0000	0,1689
IMG46	0,0133	0,0000	0,0000	0,1156
ERROR P/ ANN (%)	DEFAULT	EXCESS	DEFAULT	EXCESS
	2,3778	0,8556	0,0778	7,8889

TOTAL ERROR P/ ANN (%)	3,2333	7,9667

Table 7.5 - Data of red channel characteristics before contrast and brightness correction.

IMG	ERROR			
	RED			
	PIXEL		LOW VALUE	
	Extremely High	225	Extremely High	225
	FP	FN	FP	FN
IMG1	0,0000	0,0178	0,0000	0,0178
IMG2	0,0000	0,0889	0,0000	0,0356
IMG3	0,0044	0,0222	0,0000	0,0222
IMG4	0,0222	0,0222	0,0133	0,0178
IMG5	0,0089	0,0311	0,0044	0,0222
IMG7	0,0000	0,0533	0,0000	0,0311
IMG8	0,0044	0,0400	0,0000	0,0356
IMG9	0,0000	0,0311	0,0000	0,0267
IMG10	0,0044	0,0444	0,0000	0,0356
IMG11	0,0000	0,0178	0,0000	0,0133
IMG12	0,0000	0,0267	0,0000	0,0267
IMG13	0,0133	0,0222	0,0133	0,0133
IMG16	0,0400	0,0178	0,0222	0,0133
IMG17	0,0000	0,0311	0,0000	0,0222
IMG19	0,0400	0,0356	0,0222	0,0356
IMG20	0,0089	0,0356	0,0000	0,0222
IMG21	0,0044	0,0222	0,0044	0,0044
IMG22	0,0356	0,0133	0,0133	0,0133
IMG23	0,0400	0,0178	0,0133	0,0178
IMG24	0,0000	0,0000	0,0000	0,0000
IMG25	0,0000	0,0133	0,0000	0,0089
IMG26	0,0000	0,0578	0,0000	0,0400
IMG27	0,0000	0,0400	0,0000	0,0311
IMG28	0,0000	0,0311	0,0000	0,0222
IMG29	0,0000	0,0356	0,0000	0,0222
IMG30	0,0444	0,0222	0,0133	0,0133
IMG31	0,0044	0,0356	0,0000	0,0178

IMG32	0,0000	0,0133	0,0000	0,0089
IMG33	0,0000	0,0178	0,0000	0,0133
IMG34	0,0044	0,0444	0,0044	0,0311
IMG35	0,0222	0,0133	0,0044	0,0089
IMG36	0,0000	0,0133	0,0000	0,0089
IMG37	0,0000	0,0267	0,0000	0,0356
IMG38	0,0000	0,0222	0,0000	0,0222
IMG39	0,0000	0,0400	0,0000	0,0222
IMG40	0,0000	0,0222	0,0000	0,0222
IMG42	0,0000	0,0533	0,0000	0,0222
IMG43	0,0000	0,0622	0,0000	0,0400
IMG44	0,0000	0,1200	0,0000	0,0622
IMG46	0,0311	0,0000	0,0222	0,0000
ERROR P/ ANN (%)	DEFAULT	EXCESS	DEFAULT	EXCESS
	0,8333	3,1889	0,3778	2,2000
TOTAL ERROR P/ ANN (%)	4,0222		2,5778	

Table 7.6 - False Positive and Negative error per image data before contrast and brightness correction.

ERROR P/ IMG	FALSE POSITIVE ERROR P/ IMG	FALSE NEGATIVE ERROR P/ IMG
3,878	0,2667	3,6111
5,778	0,0000	5,7778
4,500	1,0667	3,4333
5,083	1,2056	3,8778
5,261	0,9778	4,2833
6,006	0,0889	5,9167
5,339	0,5333	4,8056
3,539	0,0000	3,5389
6,533	1,6000	4,9333
2,928	0,0000	2,9278
4,400	0,9778	3,4222
3,478	0,8500	2,6278
4,683	3,3389	1,3444
3,489	0,2667	3,2222
7,622	3,4889	4,1333

4,083	0,3556	3,7278
3,778	0,7611	3,0167
3,578	1,3833	2,1944
4,872	1,8278	3,0444
0,850	0,1778	0,6722
2,828	0,2667	2,5611
5,722	0,2667	5,4556
5,033	0,0000	5,0333
5,161	0,6222	4,5389
5,111	0,5333	4,5778
4,489	1,2444	3,2444
4,833	1,1556	3,6778
1,611	0,0000	1,6111
4,083	1,7778	2,3056
5,233	1,0667	4,1667
3,567	1,3444	2,2222
2,244	0,6222	1,6222
5,467	0,2778	5,1889
3,500	0,2667	3,2333
4,211	0,6222	3,5889
3,628	0,7111	2,9167
6,756	0,0000	6,7556
6,644	0,0000	6,6444
10,206	0,0000	10,2056
4,894	2,5833	2,3111
AVG ERROR P/IMG	AVG ERROR P/IMG	
4,623	4,3286	

Table 7.7 - Data of the green channel and magnitude FFT characteristics after contrast and brightness correction.

<table>
<tr><td rowspan="5">IMG</td><td colspan="6">ERROR</td></tr>
<tr><td colspan="3">GREEN</td><td colspan="3" rowspan="2">MAGNITUDE</td></tr>
<tr><td colspan="3">PIXEL</td></tr>
<tr><td>Extremely High</td><td>225</td><td>C=-25; B=-20</td><td>Extremely High</td><td>225</td><td>C=-75; B=0.7</td></tr>
<tr><td>DEFAULT</td><td colspan="2">EXCESS</td><td>DEFAULT</td><td colspan="2">EXCESS</td></tr>
<tr><td>IMG1</td><td>0,0044</td><td colspan="2">0,0000</td><td>0,0000</td><td colspan="2">0,0267</td></tr>
<tr><td>IMG2</td><td>0,0000</td><td colspan="2">0,0267</td><td>0,0000</td><td colspan="2">0,0400</td></tr>
<tr><td>IMG3</td><td>0,0089</td><td colspan="2">0,0133</td><td>0,0044</td><td colspan="2">0,0267</td></tr>
</table>

IMG4	0,0089	0,0311	0,0133	0,0311
IMG5	0,0133	0,0089	0,0044	0,0222
IMG7	0,0000	0,0133	0,0000	0,0267
IMG8	0,0000	0,0222	0,0000	0,0356
IMG9	0,0000	0,0222	0,0000	0,0178
IMG10	0,0267	0,0267	0,0044	0,0267
IMG11	0,0000	0,0267	0,0000	0,0178
IMG12	0,0133	0,0089	0,0000	0,0222
IMG13	0,0000	0,0400	0,0000	0,0267
IMG16	0,0267	0,0133	0,0311	0,0089
IMG17	0,0000	0,0178	0,0000	0,0222
IMG19	0,0267	0,0178	0,0267	0,0267
IMG20	0,0000	0,0222	0,0000	0,0267
IMG21	0,0089	0,0089	0,0089	0,0133
IMG22	0,0000	0,0133	0,0133	0,0178
IMG23	0,0044	0,0356	0,0222	0,0222
IMG24	0,0000	0,0000	0,0000	0,0000
IMG25	0,0044	0,0222	0,0000	0,0267
IMG26	0,0000	0,0222	0,0000	0,0356
IMG27	0,0000	0,0133	0,0000	0,0356
IMG28	0,0133	0,0089	0,0000	0,0311
IMG29	0,0133	0,0311	0,0000	0,0400
IMG30	0,0000	0,0222	0,0222	0,0178
IMG31	0,0178	0,0089	0,0133	0,0178
IMG32	0,0000	0,0178	0,0000	0,0178
IMG33	0,0400	0,0000	0,0178	0,0178
IMG34	0,0089	0,0044	0,0000	0,0178
IMG35	0,0000	0,0178	0,0044	0,0089
IMG36	0,0000	0,0000	0,0000	0,0000
IMG37	0,0000	0,0903	0,0000	0,0356
IMG38	0,0000	0,0044	0,0000	0,0222
IMG39	0,0000	0,0133	0,0000	0,0267
IMG40	0,0089	0,0000	0,0044	0,0133
IMG42	0,0000	0,0044	0,0000	0,0444
IMG43	0,0000	0,0222	0,0000	0,0622
IMG44	0,0000	0,0267	0,0000	0,0533
IMG46	0,0000	0,0000	0,0000	0,0356
ERROR P/ ANN (%)	DEFAULT	EXCESS	DEFAULT	EXCESS
	0,6222	1,7479	0,4778	2,5444

TOTAL ERROR P/ ANN (%)	2,3701	3,0222

Table 7.8 - Data of the red channel characteristics after contrast and brightness correction.

IMG	ERROR			
	RED			
	PIXEL		LOW VALUE	
	Extremely High	225 C=-50; B=-20	Extremely High	225 C=-75; B=0.8
	DEFAULT	EXCESS	DEFAULT	EXCESS
IMG1	0,0000	0,0222	0,0000	0,0044
IMG2	0,0000	0,0400	0,0000	0,0133
IMG3	0,0000	0,0178	0,0000	0,0089
IMG4	0,0044	0,0311	0,0133	0,0133
IMG5	0,0000	0,0444	0,0044	0,0133
IMG7	0,0000	0,0311	0,0000	0,0089
IMG8	0,0000	0,0311	0,0000	0,0133
IMG9	0,0000	0,0267	0,0000	0,0222
IMG10	0,0000	0,0356	0,0044	0,0133
IMG11	0,0000	0,0178	0,0000	0,0089
IMG12	0,0000	0,0178	0,0000	0,0133
IMG13	0,0044	0,0133	0,0089	0,0089
IMG16	0,0178	0,0178	0,0222	0,0044
IMG17	0,0000	0,0222	0,0000	0,0044
IMG19	0,0089	0,0444	0,0311	0,0178
IMG20	0,0000	0,0356	0,0000	0,0178
IMG21	0,0000	0,0222	0,0178	0,0044
IMG22	0,0267	0,0178	0,0222	0,0089
IMG23	0,0178	0,0133	0,0133	0,0044
IMG24	0,0000	0,0000	0,0000	0,0000
IMG25	0,0000	0,0222	0,0000	0,0000
IMG26	0,0000	0,0578	0,0000	0,0267
IMG27	0,0000	0,0356	0,0000	0,0356
IMG28	0,0000	0,0444	0,0000	0,0133
IMG29	0,0000	0,0489	0,0000	0,0178
IMG30	0,0133	0,0222	0,0222	0,0044
IMG31	0,0044	0,0267	0,0000	0,0089
IMG32	0,0000	0,0178	0,0000	0,0044
IMG33	0,0000	0,0178	0,0000	0,0133

IMG34	0,0000	0,0267	0,0000	0,0178
IMG35	0,0044	0,0089	0,0044	0,0044
IMG36	0,0000	0,0089	0,0000	0,0000
IMG37	0,0000	0,0267	0,0000	0,0089
IMG38	0,0000	0,0222	0,0000	0,0133
IMG39	0,0000	0,0267	0,0000	0,0178
IMG40	0,0000	0,0222	0,0000	0,0044
IMG42	0,0000	0,0356	0,0000	0,0044
IMG43	0,0000	0,0489	0,0000	0,0133
IMG44	0,0000	0,0578	0,0000	0,0267
IMG46	0,0089	0,0000	0,0178	0,0000
ERROR P/ ANN (%)	DEFAULT	EXCESS	DEFAULT	EXCESS
	0,2778	2,7000	0,4556	1,1000
TOTAL ERROR P/ ANN (%)	2,9778		1,5556	

Table 7.9 - False Positive and Negative error per image after contrast and brightness correction.

IMG	SUMMED ERROR P/ IMG	FALSE POSITVE ERROR P/ IMG	FALSE NEGATIVE ERROR P/ IMG
IMG1	1,850	0,0889	1,7611
IMG2	2,400	0,0000	2,4000
IMG3	2,433	0,2667	2,1667
IMG4	4,044	0,9389	3,1056
IMG5	2,917	0,4444	2,4722
IMG7	2,711	0,0000	2,7111
IMG8	2,739	0,0000	2,7389
IMG9	2,472	0,0000	2,4722
IMG10	3,589	0,7111	2,8778
IMG11	2,117	0,0000	2,1167
IMG12	1,928	0,2667	1,6611
IMG13	2,600	0,2667	2,3333
IMG16	3,261	2,0944	1,1667
IMG17	1,750	0,0000	1,7500
IMG19	5,039	2,2833	2,7556

IMG20	2,878	0,0000	2,8778
IMG21	2,522	0,8500	1,6722
IMG22	3,094	1,6611	1,4333
IMG23	3,083	1,2944	1,7889
IMG24	0,000	0,0000	0,0000
IMG25	1,928	0,0889	1,8389
IMG26	3,678	0,0000	3,6778
IMG27	3,094	0,0000	3,0944
IMG28	3,333	0,2667	3,0667
IMG29	3,856	0,2667	3,5889
IMG30	3,322	1,1556	2,1667
IMG31	2,928	1,1278	1,8000
IMG32	1,433	0,0000	1,4333
IMG33	2,967	1,1556	1,8111
IMG34	3,317	0,1778	3,1389
IMG35	1,344	0,5444	0,8000
IMG36	0,456	0,0000	0,4556
IMG37	3,783	0,1389	3,6444
IMG38	1,800	0,0000	1,8000
IMG39	2,106	0,0000	2,1056
IMG40	1,761	0,2667	1,4944
IMG42	3,167	0,0000	3,1667
IMG43	3,767	0,0000	3,7667
IMG44	5,094	0,0000	5,0944
IMG46	2,078	1,3667	0,7111
	AVG ERROR P/IMG	AVG ERROR P/IMG	
	2,716	2,8428	

Table 7.10 - Final data of FP, FN, TP and TN of all images.

ERROR

RED LOW VALUE	RED PIXEL	GREEN PIXEL	MAGNITUDE	RED LOW VALUE	RED PIXEL	GREEN PIXEL	MAGNITUDE

FINAL

Ultra High	400	Ultra High	401
False Positive	False Negative	True Positive	True Negative
0,0000	2,0000	222,0000	176,0000
0,0000	11,0000	206,0000	183,0000

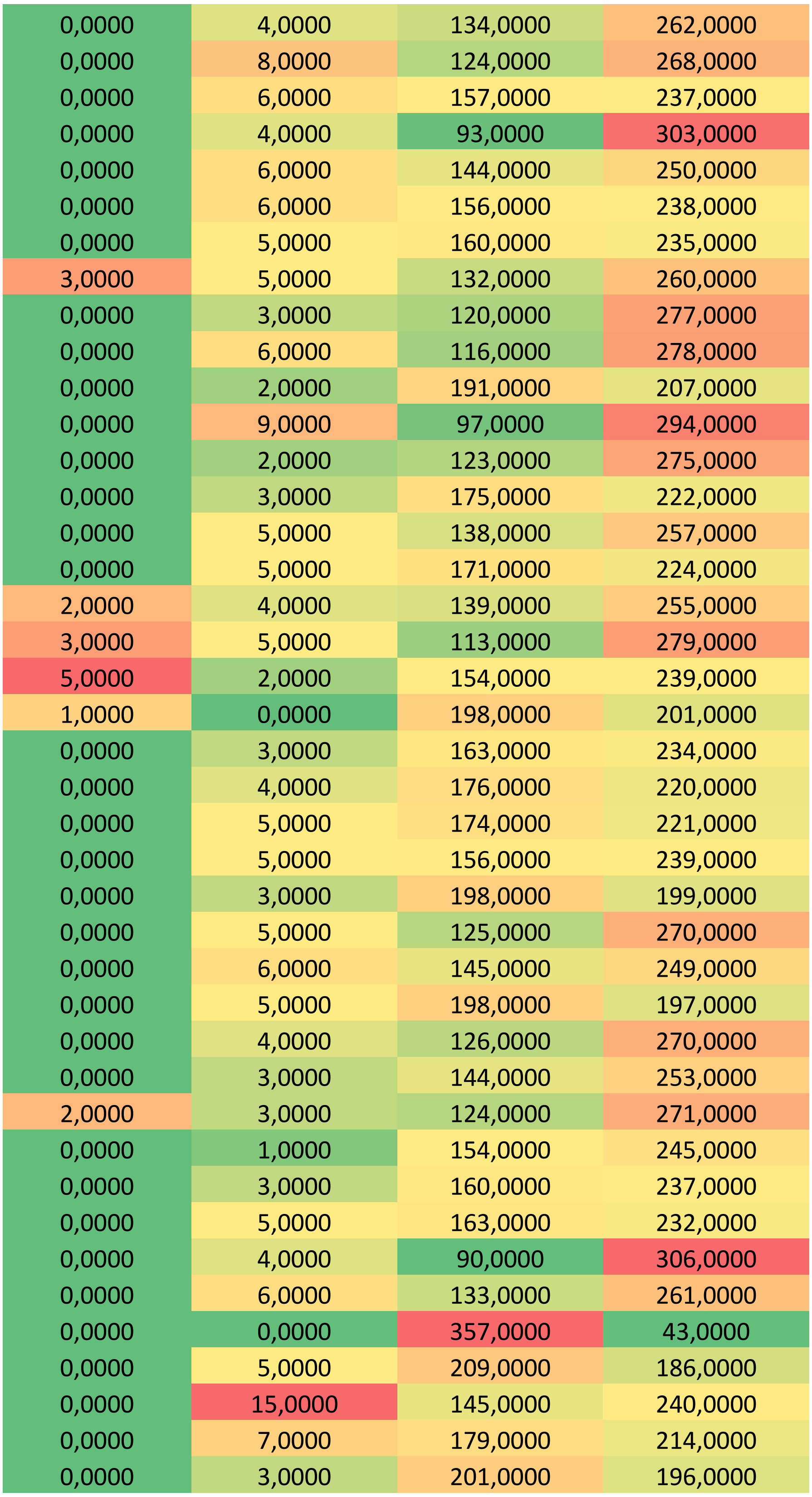

0,0000	4,0000	134,0000	262,0000
0,0000	8,0000	124,0000	268,0000
0,0000	6,0000	157,0000	237,0000
0,0000	4,0000	93,0000	303,0000
0,0000	6,0000	144,0000	250,0000
0,0000	6,0000	156,0000	238,0000
0,0000	5,0000	160,0000	235,0000
3,0000	5,0000	132,0000	260,0000
0,0000	3,0000	120,0000	277,0000
0,0000	6,0000	116,0000	278,0000
0,0000	2,0000	191,0000	207,0000
0,0000	9,0000	97,0000	294,0000
0,0000	2,0000	123,0000	275,0000
0,0000	3,0000	175,0000	222,0000
0,0000	5,0000	138,0000	257,0000
0,0000	5,0000	171,0000	224,0000
2,0000	4,0000	139,0000	255,0000
3,0000	5,0000	113,0000	279,0000
5,0000	2,0000	154,0000	239,0000
1,0000	0,0000	198,0000	201,0000
0,0000	3,0000	163,0000	234,0000
0,0000	4,0000	176,0000	220,0000
0,0000	5,0000	174,0000	221,0000
0,0000	5,0000	156,0000	239,0000
0,0000	3,0000	198,0000	199,0000
0,0000	5,0000	125,0000	270,0000
0,0000	6,0000	145,0000	249,0000
0,0000	5,0000	198,0000	197,0000
0,0000	4,0000	126,0000	270,0000
0,0000	3,0000	144,0000	253,0000
2,0000	3,0000	124,0000	271,0000
0,0000	1,0000	154,0000	245,0000
0,0000	3,0000	160,0000	237,0000
0,0000	5,0000	163,0000	232,0000
0,0000	4,0000	90,0000	306,0000
0,0000	6,0000	133,0000	261,0000
0,0000	0,0000	357,0000	43,0000
0,0000	5,0000	209,0000	186,0000
0,0000	15,0000	145,0000	240,0000
0,0000	7,0000	179,0000	214,0000
0,0000	3,0000	201,0000	196,0000

Table 7.11 - Full data of specificity, sensitivity, accuracy, precision, PPV and NNV values of all images.

SENSTIIVITY P/ IMG	SPECIFICITY P/ IMG	ACCURACY P/ IMG	PRECISION P/ IMG	POSITIVE PREDICTIVE VALUE P/ IMG	NEGATIVE PREDICTIVE VALUE P/ IMG
0,991	1,000	0,995	1,000	1,000	0,989
0,949	1,000	0,973	1,000	1,000	0,943
0,971	1,000	0,990	1,000	1,000	0,985
0,939	1,000	0,980	1,000	1,000	0,971
0,963	1,000	0,985	1,000	1,000	0,975
0,959	1,000	0,990	1,000	1,000	0,987
0,960	1,000	0,985	1,000	1,000	0,977
0,963	1,000	0,985	1,000	1,000	0,975
0,970	1,000	0,988	1,000	1,000	0,979
0,964	0,989	0,980	0,978	0,978	0,981
0,976	1,000	0,993	1,000	1,000	0,989
0,951	1,000	0,985	1,000	1,000	0,979
0,990	1,000	0,995	1,000	1,000	0,990
0,915	1,000	0,978	1,000	1,000	0,970
0,984	1,000	0,995	1,000	1,000	0,993
0,983	1,000	0,993	1,000	1,000	0,987
0,965	1,000	0,988	1,000	1,000	0,981
0,972	1,000	0,988	1,000	1,000	0,978
0,972	0,992	0,985	0,986	0,986	0,985
0,958	0,989	0,980	0,974	0,974	0,982
0,987	0,980	0,983	0,969	0,969	0,992
1,000	0,995	0,998	0,995	0,995	1,000
0,982	1,000	0,993	1,000	1,000	0,987
0,978	1,000	0,990	1,000	1,000	0,982
0,972	1,000	0,988	1,000	1,000	0,978
0,969	1,000	0,988	1,000	1,000	0,980
0,985	1,000	0,993	1,000	1,000	0,985
0,962	1,000	0,988	1,000	1,000	0,982
0,960	1,000	0,985	1,000	1,000	0,976
0,975	1,000	0,988	1,000	1,000	0,975
0,969	1,000	0,990	1,000	1,000	0,985
0,980	1,000	0,993	1,000	1,000	0,988
0,976	0,993	0,988	0,984	0,984	0,989
0,994	1,000	0,998	1,000	1,000	0,996
0,982	1,000	0,993	1,000	1,000	0,988

0,970	1,000	0,988	1,000	1,000	0,979
0,957	1,000	0,990	1,000	1,000	0,987
0,957	1,000	0,985	1,000	1,000	0,978
1,000	1,000	1,000	1,000	1,000	1,000
0,977	1,000	0,988	1,000	1,000	0,974
0,906	1,000	0,963	1,000	1,000	0,941
0,962	1,000	0,983	1,000	1,000	0,968
0,985	1,000	0,993	1,000	1,000	0,985
96,928%	99,854%	98,756%	99,733%	99,733%	98,121%